LUND UNIVERSITY

Methodological improvements in quantitative MRI

Perfusion estimation and partial volume considerations

Ahlgren, André

2017

Methodological improvements in quantitative MRI

Perfusion estimation and partial volume considerations

ANDRÉ AHLGREN
DEPARTMENT OF MEDICAL RADIATION PHYSICS | LUND UNIVERSITY 2017

Methodological improvements in quantitative MRI

Methodological improvements in quantitative MRI

Perfusion estimation and partial volume considerations

by André Ahlgren

LUND
UNIVERSITY

Thesis for the degree of Doctor of Philosophy
Thesis advisors: Linda Knutsson, Ronnie Wirestam and Freddy Ståhlberg
Faculty opponent: Associate Professor Michael Chappell, Institute of Biomedical Engineering, Department of Engineering Science, University of Oxford, UK

To be presented, with the permission of the Faculty of Science of Lund University, for public criticism in lecture hall F3, Skåne University Hospital, Lund, on Friday the 17th of February 2017 at 09:00.

Organization	Document name
LUND UNIVERSITY Department of Medical Radiation Physics Barngatan 2:1 SE–221 85 LUND Sweden	**Doctoral Thesis**
	Date of disputation 2017-02-17
	Sponsoring organization
Author(s) André Ahlgren	

Title and subtitle

Methodological improvements in quantitative MRI: Perfusion estimation and partial volume considerations

Abstract

The magnetic resonance imaging (MRI) scanner is a remarkable medical imaging device, capable of producing detailed images of the inside of the body. In addition to imaging internal tissue structures, the scanner can also be used to measure various properties of the tissue. If a tissue property is measured in every image pixel, the resulting property image (the parameter map) can be displayed and used for medical interpretation — a concept referred to as 'quantitative MRI'. Tissue properties that are commonly probed include traditional MR parameters such as T1, T2 and proton density, as well as functional parameters such as tissue perfusion, brain activation, diffusion and flow.

Quantitative MRI relies on the continuous development of new and improved ways to acquire data with the scanner (pulse sequences), to model and analyze the data (post-processing), and to interpret the output from a medical perspective. This thesis describes methods that have been developed with the specific aim to improve certain quantitative MRI techniques. In particular, the work is focused on improved analysis of perfusion MRI data, and ways to handle the partial volume issue.

Constant delivery of oxygen and nutrients via the blood is vital for tissue viability. Perfusion MRI is designed to measure the properties of the local blood delivery, and perfusion images can be used as a marker for tissue health. Whereas rough estimates of perfusion properties can suffice in some cases, more accurate information can provide improved medical research and diagnostics. Most of the methods described in this work aim to provide tissue perfusion information with higher accuracy than previous approaches.

One particular way to improve perfusion information is to account for the so-called partial volume effect. This means that limited image resolution implies that a single pixel may contain signal from more than one type of tissue. In other words, the signal can be mixed, and the calculated perfusion represents a mixture of the underlying perfusion of the different tissue types. By first using another quantitative MRI method that estimates the partial volume of each tissue type in every pixel (referred to as partial volume mapping), the partial volume effect can be corrected for by so-called partial volume correction.

Partial volume mapping also relates to the field of MRI segmentation, that is, methods to segment an image into different tissue types and anatomical regions. This work also explores and expands a new partial volume mapping and segmentation method, referred to as fractional signal modeling, which seems to be exceptionally versatile and robust, as well as simple to implement and use. A general framework is laid out, with the hope of inspiring more researchers to adapt it and assess its value in different applications.

Key words

Classification system and/or index terms (if any)

Supplementary bibliographical information	Language English
ISSN and key title	ISBN 978-91-7753-098-5 (print) 978-91-7753-099-2 (pdf)
Recipient's notes	Number of pages / Price Security classification

Methodological improvements in quantitative MRI

Perfusion estimation and partial volume considerations

by André Ahlgren

LUND
UNIVERSITY

A doctoral thesis at a university in Sweden takes either the form of a single, cohesive research study (monograph) or a summary of research papers (compilation thesis), which the doctoral student has written alone or together with one or several other author(s).

In the latter case the thesis consists of two parts. An introductory text puts the research work into context and summarizes the main points of the papers. Then, the research publications themselves are reproduced, together with a description of the individual contributions of the authors. The research papers may either have been already published or are manuscripts at various stages (in press, submitted, or in draft).

Cover illustration: Voxels with mixed tissue perfusion information due to the partial volume effect.

Hippocratic illustration: John Atkinson, *http://wronghands1.com*.

Funding information: The thesis work was financially supported by the Swedish Research Council, the Swedish Cancer Society, the Crafoord foundation, the Lund University Hospital Donation Funds, the Swedish Foundation for Strategic Research, and CR Development.

Made with LyX, based on the LaTeX thesis template by Daniel Michalik, Berry Holl, Helene Jönsson and Jonas Palm.

Faculty of Science, Department of Medical Radiation Physics

ISBN: 978-91-7753-098-5 (print)
ISBN: 978-91-7753-099-2 (pdf)

Printed in Sweden by Media-Tryck, Lund University, Lund 2017

Ars longa, vita brevis
— Hippocrates

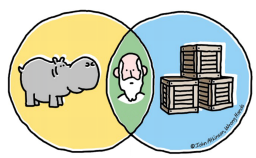

Popular summary

The magnetic resonance imaging (MRI) scanner is a remarkable medical imaging device, capable of producing detailed images of the inside of the body. In addition to imaging internal tissue structures, the scanner can also be used to measure various properties of the tissue. If a tissue property is measured in every image pixel, the resulting property image (the parameter map) can be displayed and used for medical interpretation — a concept referred to as 'quantitative MRI'. Tissue properties that are commonly probed include traditional MR parameters such as T1, T2 and proton density, as well as functional parameters such as tissue perfusion, brain activation, diffusion and flow.

Quantitative MRI relies on the continuous development of new and improved ways to acquire data with the scanner (pulse sequences), to model and analyze the data (post-processing), and to interpret the output from a medical perspective. This thesis describes methods that have been developed with the specific aim to improve certain quantitative MRI techniques. In particular, the work is focused on improved analysis of perfusion MRI data, and ways to handle the partial volume issue.

Constant delivery of oxygen and nutrients via the blood is vital for tissue viability. Perfusion MRI is designed to measure the properties of the local blood delivery, and perfusion images can be used as a marker for tissue health. Whereas rough estimates of perfusion properties can suffice in some cases, more accurate information can provide improved medical research and diagnostics. Most of the methods described in this work aim to provide tissue perfusion information with higher accuracy than previous approaches.

One particular way to improve perfusion information is to account for the so-called partial volume effect. This means that limited image resolution implies that a single pixel may contain signal from more than one type of tissue. In other words, the signal can be mixed, and the calculated perfusion represents a mixture of the underlying perfusion of the different tissue types. By first using another quantitative MRI method that estimates the partial volume of each tissue type in every pixel (referred to as partial volume mapping), the partial volume effect can be corrected for by so-called partial volume correction.

Partial volume mapping also relates to the field of MRI segmentation, that is, methods to segment an image into different tissue types and anatomical regions. This work also explores and expands a new partial volume mapping and segmentation method, referred to as fractional signal modeling, which seems to be exceptionally versatile and robust, as well as simple to implement and use. A general framework is laid out, with the hope of inspiring more researchers to adapt it and assess its value in different applications.

In conclusion, this work improved the quantification in different perfusion MRI methods, as well as presented a new partial volume mapping method. The described methods will hopefully yield value in medical applications in the future.

Populärvetenskaplig sammanfattning

Magnetkameran är en fantastisk medicinsk bildutrustning som kan producera detaljerade bilder av insidan av kroppen. Förutom bilder av vävnaden och dess struktur så kan magnetkameran också användas till att mäta olika egenskaper hos vävnaden. Om en vävnadsegenskap mäts i varje bildpixel så kan den resulterande bilden (parameterkartan) visas och användas för medicinsk bedömning, vilket kallas för kvantitativ magnetresonansavbildning (kvantitativ MRI). Vävnadsegenskaper som vanligtvis mäts inkluderar traditionella MR-parametrar såsom T1, T2 och protontäthet (PD), men även funktionella parametrar såsom vävnadsperfusion, hjärnaktivitet, diffusion och flöde.

Kvantitativ MRI kräver kontinuerlig utveckling av nya och förbättrade metoder för insamling av data (pulssekvenser), för modellering och bearbetning av data, och för att tolka resultaten ur ett medicinskt perspektiv. Denna avhandling beskriver nyutvecklade metoder, specifikt framtagna för att förbättra resultaten inom vissa kvantitativa MRI-tekniker. Mer specifikt så har arbetet fokuserat på förbättrad bearbetning av perfusions-MRI-data samt metoder för att hantera svårigheten med partiella volymer.

Konstant inflöde av syre och näring via blodet är avgörande för att vävnaden ska fungera. Perfusions-MRI är en teknik för att mäta det regionala inflödet av blod, och perfusionsbilderna kan användas för att utvärdera vävnadens hälsotillstånd. Även om ungefärliga perfusionsvärden kan vara tillräckligt i vissa fall, så kan mer korrekta värden öppna möjligheter för bättre medicinsk forskning och diagnostik. Därför var ett centralt syfte med detta avhandlingsarbete att utvärdera alternativa metoder som kan tillhandahålla mer korrekta perfusionsvärden.

Ett sätt att förbättra perfusionsmätningar är att korrigera för den så kallade partialvolymseffekten, det vill säga att begränsad bildupplösning medför att en bildpixel kan innehålla signal från flera olika vävnadstyper. Det betyder att signalen kan vara blandad, och det beräknade perfusionsvärdet motsvarar en blandning av den faktiska perfusionen för de olika vävnadstyperna. Genom att först använda en annan kvantitativ MRI-metod som mäter volymen av varje vävnadstyp i alla pixlar (kallas partialvolymsmätning), så kan partialvolymseffekten korrigeras genom så kallad partialvolymskorrigering.

Partialvolymsmätning relaterar även till så kallad MRI-segmentering, vilket betyder att dela upp en bild i olika vävnadstyper. I detta arbete utvärderades och expanderades även en ny metod för partialvolymsmätning och segmentering. Metoden visade sig vara mycket användbar och robust, och samtidigt enkel att använda. En generell beskrivning presenteras i denna avhandling, med förhoppningen att fler forskare ska kunna implementera och utvärdera metoden och undersöka dess potential i olika applikationer.

Sammanfattningsvis presenterar detta arbete förbättringar inom kvantitativ perfusions-MRI, liksom vidareutveckling av en ny metod för partialvolymsmätning. Metoderna kommer förhoppningsvis vara värdefulla för medicinska applikationer i framtiden.

List of original papers

This thesis is based on the following papers, referred to by Roman numerals:

I **Perfusion quantification by model-free arterial spin labeling using nonlinear stochastic regularization deconvolution**

André Ahlgren, Ronnie Wirestam, Esben Thade Petersen, Freddy Ståhlberg and Linda Knutsson
Magnetic Resonance in Medicine 2013;70(5):1470–1480

II **Partial volume correction of brain perfusion estimates using the inherent signal data of time-resolved arterial spin labeling**

André Ahlgren, Ronnie Wirestam, Esben Thade Petersen, Freddy Ståhlberg and Linda Knutsson
NMR in Biomedicine 2014;27(9):1112–1122

III **A linear mixed perfusion model for tissue partial volume correction of perfusion estimates in dynamic susceptibility contrast MRI: Impact on absolute quantification, repeatability and agreement with pseudo-continuous arterial spin labeling**

André Ahlgren, Ronnie Wirestam, Emelie Lind, Freddy Ståhlberg and Linda Knutsson
Magnetic Resonance in Medicine 2016;doi:10.1002/mrm.26305

IV **Automatic brain segmentation using fractional signal modeling of a multiple flip angle, spoiled gradient-recalled echo acquisition**

André Ahlgren, Ronnie Wirestam, Freddy Ståhlberg and Linda Knutsson
Magnetic Resonance Materials in Physics, Biology and Medicine 2014;27(6):551–565

V **Quantification of microcirculatory parameters by joint analysis of flow-compensated and non-flow-compensated intravoxel incoherent motion (IVIM) data**

André Ahlgren, Linda Knutsson, Ronnie Wirestam, Markus Nilsson, Freddy Ståhlberg, Daniel Topgaard and Samo Lasič
NMR in Biomedicine 2016;29(5):640–649

List of contributions

Paper I

I implemented the method and performed the analysis. I was the main author of the manuscript.

Paper II

I conceptualized the project, implemented the method and performed the analysis. I was the main author of the manuscript.

Paper III

I assisted in the data collection, implemented the method, performed the analysis and was the main author of the manuscript.

Paper IV

I conceived the partial volume mapping method and designed the study. I acquired the data, implemented the method, performed the analysis and was the main author of the manuscript.

Paper V

I acquired the data, implemented the method, performed the analysis and was the main author of the manuscript.

Summary of papers

Paper I

Deconvolution methods in model-free arterial spin labeling

Arterial spin labeling (ASL) perfusion quantification is usually accomplished using single time-point data and parametric modelling of the microvascular blood flow. In model-free ASL on the other hand, arterial and tissue signals are dynamically sampled, and subsequent deconvolution yields model-free perfusion estimates (Petersen et al., 2006). In Paper I, different deconvolution methods were compared for model-free ASL. In particular, singular value decomposition (SVD) deconvolution was compared with nonlinear stochastic regularization (NSR) deconvolution. NSR produced more realistic deconvolution results and was less prone to perfusion underestimation, compared to SVD. The paper also included the use of T_1 information for partial volume mapping, a concept that was further exploited and expanded in Papers II–IV.

Paper II

Partial volume correction in model-free arterial spin labeling

Partial volume correction (PVC) has been suggested to be an important post-processing step for ASL perfusion imaging, especially when separation of tissue volume and perfusion alteration is warranted. PVC in ASL relies on intravoxel partial volume (PV) estimates of different tissue types, and most studies have used registration of segmentation results from a high-resolution morphological scan as a proxy measure for PVs. In Paper II, we exploited the fact that the dynamic ASL sequence (used in Paper I) allows for PV mapping in the native low-resolution space of the ASL data. Hence, PVC was accomplished with the inherent ASL data only, that is, without registration or additional scans. The stuy demonstrated that the methodology can produce good PVC results in line with, or better than, the conventional approach.

Paper III

Tissue partial volume correction in dynamic susceptibility contrast MRI

Partial volume effects (PVEs) and PVC algorithms have been assessed in ASL perfusion imaging. In Paper III, we aimed to establish the impact of PVEs in dynamic susceptibility contrast MRI (DSC-MRI), and to propose a corresponding simplified post-hoc PVC method. Several simplifications yielded a mixed perfusion model identical to the one commonly used in ASL, and established PVC algorithms could thus be applied. Errors due to the simplifications were evaluated in simulations. In vivo DSC-MRI and ASL data were used to assess the repeatability of and agreement between the perfusion modalities, with and without PVC. The simplified PVC successfully reduced PVEs in DSC-MRI, although the required assumptions introduced non-negligible uncertainties.

Paper IV

Partial volume mapping based on spoiled gradient-recalled echo data

Automatic segmentation and PV mapping based on fractional signal modelling of an inversion recovery acquisition has previously been proposed (Shin et al., 2010). This so-called FRASIER method models the signal as a linear combination of contributions from gray matter, white matter and cerebrospinal fluid. The FRASIER method was the main method for PV mapping in Papers I–III. In Paper IV we suggested that the partial signal concept can be adapted to other quantitative MRI experiments, and demonstrated this with a spoiled gradient-recalled echo acquisition with variable flip angles. Simulations were used to demonstrate the accuracy and precision of the PV maps, and initial in vivo results showed that the method performed well compared to the original FRASIER method.

Paper V

Intravoxel incoherent motion with variable flow-compensation

A intravoxel incoherent motion (IVIM) experiment is usually based on modelling the signal attenuation in diffusion weighted data as the combined effects of molecular diffusion (Brownian motion) and the psuedo-diffusion effect from blood moving through the capillary system (perfusion). In Paper V we exploited that, if blood spins do not change direction during the diffusion encoding, the dephasing due to perfusion can be refocused using flow-compensation. Hence, for sufficiently fast motion encoding, the signal attenuation due to perfusion can be turned on and off by changing the gradient waveforms of the sequence. We showed in simulations that by acquiring data at several diffusion encoding strengths (b-values) with and without flow-compensation, the IVIM parameters can be estimated with improved accuracy and precision compared to a conventional IVIM experiment. Nulling of the perfusion signal attenuation was also demonstrated for in vivo brain data.

List of common abbreviations

AIF	Arterial input function
ASL	Arterial spin labeling
CASL	Continuous arterial spin labeling
CBF	Cerebral blood flow
CBV	Cerebral blood volume
CSF	Cerebrospinal fluid
DSC-MRI	Dynamic susceptibility contrast MRI
FC	Flow compensation
FSM	Fractional signal mapping
GM	Gray matter
IR	Inversion recovery
IVIM	Intravoxel incoherent motion
MR	Magnetic resonance
MRI	Magnetic resonance imaging
MTT	Mean transit time
NC	No flow compensation
NSR	Nonlinear stochastic regularization
PASL	Pulsed arterial spin labeling
PCASL	Pseudocontinuous arterial spin labeling
PV	Partial volume
PVC	Partial volume correction
PVE	Partial volume effect
RF	Radiofrequency
ROI	Region of interest
SR	Saturation recovery
SVD	Singular value decomposition
VFA	Variable flip angle
WM	White matter

Contents

1 Introduction and aims **1**

2 Perfusion MRI **3**
Tracer kinetic modeling 4
Dynamic susceptibility contrast MRI 7
Arterial spin labeling 13

3 Partial volume mapping **21**
Segmentation 21
Fractional signal modeling 24

4 Partial volume correction in perfusion MRI **31**
The partial volume effect 31
Partial volume correction 34

5 Incoherent flow imaging **39**
Intravoxel incoherent motion 39
Spatially incoherent flow 41
General model and intermediate regime 42
Flow compensated intravoxel incoherent motion 43

6 Conclusions and future aspects **47**

Chapter 1

Introduction and aims

Quantitative magnetic resonance imaging (MRI) refers to the process of measuring and mapping an objects property, in numerical terms, using MRI. Historically, the term quantitative MRI has often been assigned to the measurement of conventional magnetic resonance (MR) parameters such as relaxation times and proton density, whereas it is used in a broader sense in this thesis [1]. In medical applications, the measurements are used to probe morphological or physiological properties of human tissue, which yields unique contrast patterns that can be used in, for example, diagnosis or treatment planning and evaluation. In addition, quantitative MRI can contribute to clinical research by aiding scientists in the study of biological processes, diseases and treatments. The possibilities in quantitative MRI seems endless, and well-established methods include, but are not limited to, measurement of relaxation times, proton density, perfusion, diffusion, flow, magnetization transfer (MT), brain activation (functional MRI; fMRI), concentration of molecules (spectroscopic methods) and tissue volumes. These techniques are continuously developed and employed in research, and are also used in specific clinical applications. While conventional morphological imaging is used to find pathologies by examining a single MR image with a certain weighting, quantitative MRI is generally based on collecting several MR images (raw data) from which maps of the properties (or parameters) of interest are calculated. Hence, quantitative MRI involves the entire process from pulse sequence development and data collection strategies to image processing, corrections, biophysical modeling, data analysis and interpretation. The possibility to measure a multitude of properties, and the existence of such a wide array of important components in the quantification processes, might explain the MR researchers' interest in testing and suggesting new and improved methods.

The advent of quantitative MRI was when the MRI scanner was no longer seen purely as a camera, and started to be used as a scientific measuring instrument [1]. In contrast to conventional morphological imaging, it is not sufficient to have good image quality and contrast. To be able to rely on and compare findings at different times, in different parts of the body, in different patients, and even between different scanners, quantitative

measurements need to show good accuracy, precision, repeatability and reproducibility. Even then, if the measurement has poor sensitivity or specificity, it might not be clinically applicable. Another important factor is the complexity and cost of the method. A robust and valuable method may still struggle to gain interest if it is difficult to implement or use, or if it has a high cost in terms of, for example, resources or time. From these perspectives, the studies presented in this thesis are focused on the assessment of accuracy, precision and repeatability of both simple and advanced, automated quantitative methods. Specifically, new techniques have been assessed in the fields of perfusion MRI and partial volume (PV) mapping.

Perfusion MRI is widely used to map various microvascular properties. The perfusion MRI methods discussed in this work are arterial spin labeling (ASL), dynamic susceptibility contrast MRI (DSC-MRI) and intravoxel incoherent motion (IVIM) imaging. Since IVIM imaging originates from diffusion MRI and employs a different type of analysis than in conventional perfusion MRI, it is discussed in a separate chapter. PV mapping is a less well-defined field, but used here to denote methods used to map volumes of different tissue types. It is related to, and can be argued to pertain to, the fields of MRI segmentation and volumetry.

In Paper I, a deconvolution algorithm is adopted from DSC-MRI to improve the perfusion quantification in model-free ASL. In Paper II, PVs are calculated from ASL raw data allowing for partial volume correction (PVC) of perfusion values in model-free ASL. In Paper III, PVC is introduced in DSC-MRI, and the results are compared with corresponding ASL results. A new PV mapping method is demonstrated and evaluated in Paper IV. Paper V presents a new IVIM analysis approach to improve the quantification of corresponding perfusion parameters. The aims of the papers were thus

I. to improve perfusion estimation in model-free ASL,

II. to incorporate and asses PVC in model-free ASL,

III. to introduce and assess PVC in DSC-MRI,

IV. to propose and assess a new PV mapping method,

V. to improve quantification in IVIM imaging.

Chapter 2

Perfusion MRI

Perfusion[1] refers to the delivery of blood to the capillary systems in the tissue. Oxygenated blood travels from the heart, through large arteries, to small arterioles, through the capillary system, and exits on the venous side. Maintaining tissue perfusion is vital since the blood carries oxygen and nutrients to the tissue, and transports carbon dioxide and waste material away from the tissue. Autoregulation mechanisms are continuously engaged to uphold the required blood delivery. Thus, perfusion is intricately coupled to, and can be seen as an indirect marker of, tissue viability and metabolism. The load and unload (exchange) of gas and substances between blood and tissue takes place in the capillary system (Figure 2.1). The capillary system, together with arterioles and venules, makes up an intricate mesh of microscopic vessels embedded in the tissue, referred to as the microvascular system. It is important to distinguish between macroscopic and microscopic blood flow, and the corresponding MR techniques. The convention is that so-called flow MR techniques are used to characterize macroscopic blood flow in large vessels, and that perfusion MRI techniques are used to characterize the capillary blood supply. Thus, perfusion MRI is often used to identify tissue with abnormal perfusion, whereas the cause may originate from elsewhere (for example, an occlusion upstream) and be better visualized with another technique.

Perfusion MRI can be used to measure different properties of the microvascular system, the most central property naturally being the perfusion. As a physical quantity, perfusion is normally described as the volume of blood flowing through the microvascular system per unit time and per volume or mass of tissue. In addition, measurement of microvascular blood volume and transit time (i.e., the time it takes for blood particles to traverse the microvascular system) is possible with certain perfusion MRI techniques, as will be described in this chapter. For additional reading on perfusion MRI, Refs. [2–7] are recommended.

[1]The word 'perfusion' comes from the French word 'perfuser' meaning 'pour over or through', and refers to the fact that the blood 'soaks' or 'pours through' the organ/tissue.

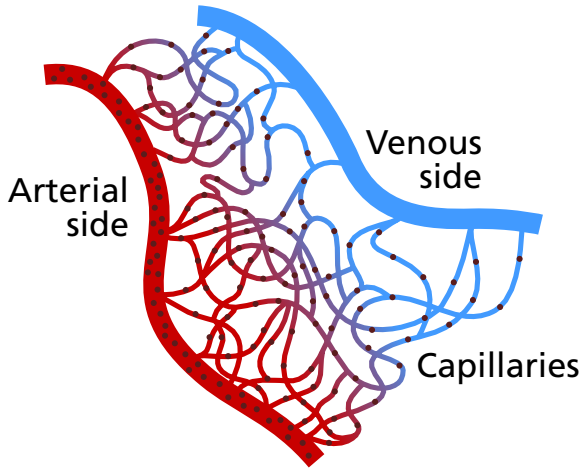

Figure 2.1: The microvascular system consists of a mesh of arterioles, capillaries and venules, resulting in multiple pathways and corresponding distribution of transit times for blood molecules traversing the system. The capillary blood constantly exchange molecules with the interstitial fluid, and this exchange is part of the delivery of oxygen and nutrients to, and removal of waste from, the tissue. Perfusion is the volume of blood delivered to the system per unit time per unit volume or mass of tissue. The blood volume is the relative volume of blood in the system, and the transit time is the time it takes for a particular blood particle to traverse the system. *Adapted from Carolina Biological Supply/Access Excellence.*

Tracer kinetic modeling

In perfusion MRI, blood is used as the carrier of a tracer or and indicator that changes the MRI signal contrast. It can be an injected contrast agent, as in DSC-MRI, or it can be magnetization (labeled blood water), as in ASL. To infer properties of the microvascular blood flow requires, in addition to data collection, biophysical modeling for analysis of the data. Although steady-state experiments based on the Kety-Schmidt formalism [8] have been applied to perfusion MRI, most current methods are based on tracer kinetic modeling according to the Meier-Zierler indicator-dilution theory [9–11]. Note that this theory is neither specific to the brain nor to perfusion MRI.

The ideal system is a simplified model with a set of assumptions that allows for derivation of very useful equations describing the tracer kinetics. The microvascular system is modeled as system with a single input and a single output, with several different pathways available for the tracer particles traversing the system. It is assumed that the tracer distribution volume V and volumetric flow rate F (flow for short) are constant during the experiment (i.e., the system is time-invariant), implying that the tracer can not be trapped in the system. The time it takes for a particle to traverse the system is referred to as the transit time. Different pathways and particle velocities results in a probability distribution of tracer transit times $h(t)$, and it is assumed that this distribution does not change during the experiment (i.e., the system is stationary). Finally, it is assumed that the system is linear and that the kinetic properties of the tracer mirrors those of the native fluid (normally blood).

The tracer concentration in arterial blood, $c_a(t)$, is the input to the system, and the tracer concentration in venous blood, $c_v(t)$, is the output. The transit time distribution $h(t)$ can also be seen as the fractional washout rate of the tracer at time t (in units s^{-1}). Thus, for an ideal impulse (infinitely short) input, $c_v(t)$ directly corresponds to $h(t)$. In real experiments, however, $c_a(t)$ is a smoothly varying function of time (Fig. 2.2). In this case, the input is convoluted upon the characteristic transit time distribution, and the output is given by

$$c_v(t) = [c_a(t) \otimes h(t)] = \int_0^t c_a(t)h(t-\tau)d\tau, \qquad [2.1]$$

where $\otimes$ denotes convolution. Equation 2.1 is known as the convolution integral, and is commonly used in signal processing and electrical engineering. It can be interpreted as follows: For a linear system, if the impulse response $h(t)$ is known, the system response (output) can be calculated for any input by convolution.

Considering an ideal impulse input, the cumulative fraction of the tracer that has left the system at time t is given by

$$H(t) = \int_0^t h(\tau)d\tau. \qquad [2.2]$$

The impulse residue function (residue function for short) $R(t)$ specifies the fraction of tracer that remains in the system at time t after an ideal impulse input. Hence, the residue function is the complement of $H(t)$, and related to the transit time distribution according to

$$R(t) = 1 - H(t) = 1 - \int_0^t h(\tau)d\tau. \qquad [2.3]$$

Since $h(t)$ is a probability distribution, it is apparent that $R(t)$ is a nonnegative monotonically decreasing function of time that fulfills $R(0) = 1$ and $\lim_{t\to\infty} R(t) = 0$ (Fig. 2.2). Note that the shapes of $h(t)$ and $R(t)$ are important since they relate to the tracer kinetic properties of the system.

The amount of tracer that remains in the system (tissue) at time t, $q_t(t)$, depends on the flow and the difference in accumulated input and output, according to

$$q_t(t) = V_t c_t(t) = F\left[\int_0^t c_a(\tau)d\tau - \int_0^t c_v(\tau)d\tau\right], \qquad [2.4]$$

where V_t is the tissue volume and $c_t(t)$ is the tracer concentration in tissue. Combination of Eqs. 2.1–2.4 yields an expression for the tissue tracer concentration according to [6, 12]

$$c_t(t) = \frac{F}{V_t}\int_0^t c_a(t)\left[1 - \int_0^t h(\upsilon)d\upsilon\right]d\tau$$
$$= f_t \int_0^t c_a(t)R(t-\tau)d\tau = f_t\left[c_a(t) \otimes R(t)\right], \quad [2.5]$$

where $f_t = F/V_t$ is the volume-specific flow, normally referred to as tissue perfusion. Equation 2.5 shows that the tissue tracer concentration is given by the convolution of the arterial tracer concentration and the residue function, scaled with tissue perfusion. The graphs in Figure 2.2 illustrate this equation, as well as the relation between $h(t)$ and $R(t)$. This is one of the most central equations in perfusion MRI, and the usefulness comes from the fact that we can measure $c_t(t)$ and $c_a(t)$ using external monitoring, and estimate f_t and $R(t)$ by means of deconvolution, i.e.,

$$f_t R(t) = c_a(t) \otimes^{-1} c_t(t), \quad [2.6]$$

where $\otimes^{-1}$ denotes deconvolution. This approach is common in DSC-MRI, whereas measurement of $c_t(t)$ and modeling of $c_a(t)$ and $R(t)$ also allows for estimation of f_t, which is common in ASL.

Equations 2.1–2.4 were well described by Zierler [11], but the first record of Eq. 2.5 is difficult to find. Lassen and Perl showed that the tracer residue in the system is given by the convolution of the input and the impulse residue function, and that the single compartment Kety model applied to washout of diffusible tracers can be written as Eq. 2.5 (although that method assumes a specific residue function) [13]. The adoption to perfusion MRI was probably inspired by work on tracer kinetic modeling in nuclear medicine and computed tomography (CT) from the early 1980's [13–15] (B. Rosen and R. Buxton, personal communication).

The tracer distribution volume can be determined by

$$V = F\int_0^\infty t\,h(t)dt = FT, \quad [2.7]$$

which was elegantly derived by Zierler using deductive reasoning [10]. The integral in Eq. 2.7 is the first moment of the transit time distribution, i.e., the mean transit time T. The fact that volume equals flow multiplied by mean transit time is known as the central volume theorem [16], which is a corollary of the Fick principle. Using Eq. 2.3, it can further be shown that

$$T = \int_0^\infty t\,h(t)dt = \int_0^\infty R(t)dt. \quad [2.8]$$

By combining Eqs. 2.5–2.8 and integrating from zero to infinity, we find a useful expression for the distribution volume fraction (volume-specific tracer distribution volume) in tissue according to

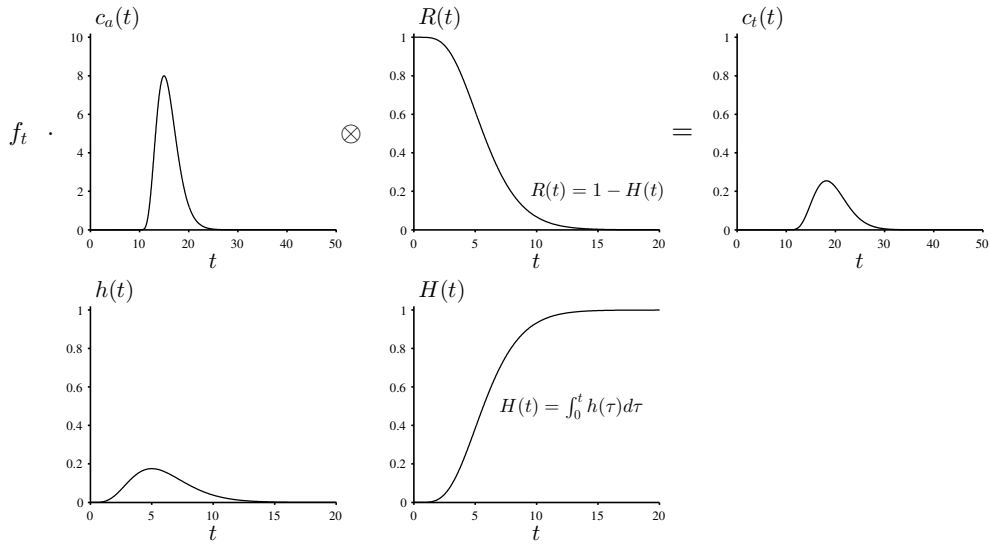

Figure 2.2: A schematic illustration of the tracer kinetic formalism used in perfusion MRI. The top row shows the perfusion-scaled convolution of the arterial tracer concentration and the residue function, equaling the tissue tracer concentration (Eq. 2.5). The bottom row shows the probability distribution and cumulative distribution of transit times, related to the residue function according to Eq. 2.3.

$$v_t = \frac{V}{V_t} = \frac{\int_0^\infty c_t(t)dt}{\int_0^\infty c_a(t)dt}. \qquad [2.9]$$

Note that, for an intravascular (nondiffusible) tracer, V is related to the blood volume.

The organ most commonly studied with perfusion MRI is the brain, although the principles described here are generally applicable to other systems as well. Note that the tracer can be intravascular as in DSC-MRI (assuming an intact blood-brain barrier), or extravascular as in ASL. The conventional quantities and units in brain perfusion MRI are cerebral blood flow (CBF) in ml blood per 100 g tissue per minute [ml/100g/min], cerebral blood volume (CBV) in ml blood per 100 g tissue [ml/100g] and mean transit time (MTT) in seconds [s]. Note that, by convention, CBF and CBV are reported in mass-specific units.

Dynamic susceptibility contrast MRI

In the late 1980s, Rosen and colleagues proposed to exploit dynamic susceptibility-induced signal changes in T2-weighted MRI sequences following an injection of a paramagnetic contrast agent for perfusion imaging [17–19]. They proposed the use of lanthanide chelates as intravascular tracers, measured the relation between signal change and tracer concentration, and proposed to use Meier-Zierler formalism with deconvolution to quantify perfusion, all of which is the basis for DSC-MRI today. Based on experimental results, they found that the signal decrease was primarily caused by the susceptibility

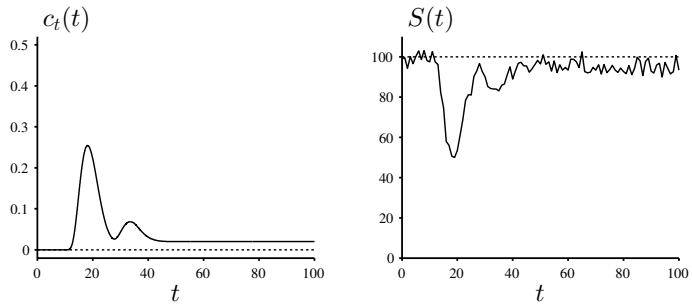

Figure 2.3: A simulated tissue contrast agent concentration curve and the corresponding DSC-MRI signal with a 50% signal drop (Eqs. 2.10–2.11). The simulation is based on the same input and system characteristics as in Figure 2.2, but with added recirculation, steady-state different from baseline, and a limited temporal resolution and measurement noise added to the signal (to mimic experimental data).

difference between the capillaries containing the contrast agent and the surrounding tissue. In the middle of the 1990s, Rempp et al. [20] and Østergaard et al. [21, 22] made seminal contributions that helped to disseminate and popularize the technique. Rempp et al. suggested a data collection and processing approach, and demonstrated the first quantitative in-vivo perfusion results with DSC-MRI [20]. Østergaard et al. stressed the importance of appropriate post-processing, and especially focused on assessing different deconvolution techniques [21, 22]. For more details on DSC-MRI, bolus-tracking and deconvolution in perfusion imaging see Refs. [12, 23, 24].

Theory

For a gradient-echo sequence, the change in MR signal $S(t)$ is related to the change in transverse relaxation rate and contrast agent concentration according to[2] [18]

$$S(t) = S_0 e^{-T_E \Delta R_2^*(t)} = S_0 e^{-T_E r_2^* c(t)}, \qquad [2.10]$$

where S_0 is the baseline signal, T_E is the echo time, $\Delta R_2^*(t) = r_2^* c(t)$ is the change in transverse relaxation rate, r_2^* is the transverse relaxivity of the contrast agent, and $c(t)$ is the contrast agent concentration (Fig. 2.3).

The proportionality factor r_2^* is geometry dependent and can thus vary with vessel diameter, between vessels and tissue, and between different tissue types. In particular, the extravascular tissue protons are dephased by susceptibility-induced magnetic fields due to the contrast agent in the blood, and has thus a fundamentally different dependence on contrast agent (higher r_2^*) than the blood [25]. Furthermore, r_2^* can vary with contrast agent concentration, effectively yielding a nonlinear relation between ΔR_2^* and c (as demonstrated in whole blood) and subsequent erroneous concentration curve shapes [26].

[2]The same relation can be used for spin-echo sequences, which would correspond to removing the * superscripts .

Even though failure to take these effects into account can lead to errors in perfusion and blood volume estimates [25], it is common to assume a global linear relationship since it enables a tractable solution to a very complicated problem.

Eq. 2.10 can be rewritten as [18]

$$r_2^* c(t) = \Delta R_2^*(t) = -\frac{1}{T_E} \ln\left(\frac{S(t)}{S_0}\right), \qquad [2.11]$$

i.e., the dynamic signal decrease is converted to a relative contrast agent concentration (Fig. 2.3). Assuming a global linear relationship, r_2^* can be divided out, which yields the DSC-MRI analogue of Eq. 2.5 according to

$$k_H c_t(t) = \rho f_t \int_0^t c_a(t) R(t-\tau) d\tau = \rho f_t \left[c_a(t) \otimes R(t)\right], \qquad [2.12]$$

where k_H is a correction factor, $c_t(t)$ is the contrast agent concentration in tissue, ρ is the brain tissue density, $f_t = F/(\rho V_t)$ is the CBF, and $c_a(t)$ is the contrast agent concentration in the feeding artery, referred to as the arterial input function (AIF). The tissue density ρ is introduced to obtain tissue perfusion in the conventional mass-specific units. The correction factor is defined as $k_H = (1 - H_{art})/(1 - H_{cap})$, where H_{art} is the arterial haematocrit (Hct) and H_{cap} is the capillary Hct, and this factor compensates for that the contrast agent only distributes in blood plasma whereas we want to calculate properties of whole blood.

Dynamic acquisition of gradient-echo or spin-echo data allows for calculation of $c_t(t)$ from the tissue of interest and $c_a(t)$ from a feeding artery, using Eq. 2.11. Deconvolution then yields the perfusion-scaled impulse residue function $R_f(t) = f_t R(t)$ (cf. Eq. 2.6). Since $R(0) = 1$ and $R(t)$ is monotonically decreasing, we obtain that

$$f_t = R_f(0) = \max[R_f(t)] \qquad [2.13]$$

and

$$R(t) = \frac{R_f(t)}{R_f(0)} = \frac{R_f(t)}{\max[R_f(t)]}. \qquad [2.14]$$

In practice, the $R_f(t)$ obtained by deconvolution might not be monotonically decreasing, and it is therefore common to use $\max[R_f(t)]$ rather than $R_f(0)$ in Eqs. 2.13 and 2.14. Calculation of MTT from the perfusion-scaled impulse residue function is known as Zierler's area-to-height relation:

$$T = \frac{\int_0^\infty R_f(t) dt}{\max[R_f(t)]}. \qquad [2.15]$$

CBV can be calculated according to (cf. Eq. 2.9)

$$v_t = k_H \frac{V}{\rho V_t} = \frac{k_H}{\rho} \frac{\int_0^\infty c_t(t) dt}{\int_0^\infty c_a(t) dt}, \qquad [2.16]$$

where the correction for Hct converts from distribution (plasma) volume fraction to whole blood volume fraction.

Finally, it should be remembered that if two out of the three parameters (f_t, v_t and T) are available, the third can be calculated using the central volume theorem, $v_t = f_t T$ (Eq. 2.7). The alternative expressions thus become

$$f_t = \frac{k_H \int_0^\infty c_t(t)dt \ \max[R_f(t)]}{\rho \int_0^\infty c_a(t)dt \ \int_0^\infty R_f(t)dt}, \qquad [2.17]$$

$$v_t = \int_0^\infty R_f(t)dt, \qquad [2.18]$$

and

$$T = \frac{k_H \int_0^\infty c_t(t)dt}{\rho \int_0^\infty c_a(t)dt \ \max[R_f(t)]}. \qquad [2.19]$$

Arterial input function

Many of the challenges in DSC-MRI are related to the AIF, as comprehensively reviewed by Calamante [27]. As mentioned previously, the relation between relaxation rate and contrast agent concentration is different for the AIFs and the tissue curves, and this is important to take into account if absolute values are warranted [25, 26, 28]. Another source of erroneous AIF registration is PVEs, and several ways to correct the AIF area have been proposed [27]. For example, in Paper III, we used the prebolus approach in which the AIF is rescaled to the area of a venous output function (VOF) acquired from a preceding single-slice prebolus experiment [29]. Another approach towards quantification in absolute terms is to use independent calibration measurements, for example, nuclear medicine based perfusion or alternative MRI measurements of CBF or CBV [5, 24, 30].

Delay and dispersion

Delay between the registered AIF and tissue curves, as well as bolus dispersion during the corresponding transit, may lead to severe CBF quantification errors [31]. The most common ways to account for delay is to use a delay-insensitive deconvolution algorithm, to account for delay in the model, or to employ local AIFs [27, 32, 33]. Bolus dispersion refers to the continuous dilution of the tracer during the transit from the site of the measured AIF to the site of the measured tissue curve, and this is a more delicate and difficult problem. It manifests itself as a broadening of the bolus, and is caused by the variation in blood velocity and the different pathways of the arterial system. A common way to model dispersion is therefore to use a vascular transport function $h_a(t)$ which, similarly to the capillary transit time probability distribution $h(t)$, is the probability distribution of transit times from the

site of the measured AIF to the tissue of interest. With this definition, if $c_a^*$is the measured AIF, the true AIF is given by $c_a(t) = c_a^*(t) \otimes h_a(t)$, and Eq. 5 can be modified to include dispersion according to

$$c_t(t) = f_t \left[c_a(t) \otimes R(t)\right] = f_t \left[c_a^*(t) \otimes h_a(t) \otimes R(t)\right] = f_t \left[c_a^*(t) \otimes R^*(t)\right] \quad [2.20]$$

where $R^*(t) = h_a(t) \otimes R(t)$ is the 'dispersed' effective residue function obtained by deconvolution if dispersion is not accounted for. Example of a vascular transport function, and the effect on the AIF and the perfusion-scaled residue function, is shown in Figure 2.4. It can be seen that arterial dispersion leads to a distorted and non-physiological residue function, with corresponding underestimation of CBF (Eq. 2.13) and overestimation of MTT (Eq. 2.15). These types of distortions are the reason why perfusion is usually estimated from $\max[R_f(t)]$ rather than $R_f(0)$.

From Eq. 2.20 it is apparent that it is very difficult to separate the effects of arterial bolus dispersion and the microvascular distribution of the bolus given by the true residue function. To improve quantification in the presence of delay and dispersion, Willats et al. proposed the use of deconvolution methods able to recover a wider array of effective residue function shapes [34, 35]. However, this does not correct for dispersion, and others have attempted to model and estimate the amount of dispersion to correct for the effect [36–38]. Several models for h_a have been suggested in the DSC-MRI and ASL literature, such as exponential [27], Gaussian [39, 40] and gamma [38, 41].

As described later, both delay and dispersion were accounted for in Paper I. In particular, delay effects were minimized by shifting signal curves prior to deconvolution, and dispersion was modeled in the form of an exponential function.

Deconvolution

Since deconvolution is a difficult operation prone to errors, some researchers have promoted the use of qualitative (descriptive or summary) parameters. However, it has been shown that deconvolution is required for reliable perfusion estimation [42, 43]. Many deconvolution methods have been proposed in the literature and a brief overview is given here (see also, for example, Refs. [7, 24]). Deconvolution methods can be divided into two groups; model dependent (parametric) and model independent (nonparametric or model-free) methods.

Assuming that the contrast agent's capillary transport can be described by an analytical function, the deconvolution can be realized by nonlinear least squares fitting. The most simple parametrization is based on the assumption of a vascular system corresponding to a single well-mixed compartment, resulting in a mono-exponential residue function model according to $R(t) = e^{-t/T}$. Another approach is to model the transit time distribution, for example using a gamma distribution [44]. Model-dependent deconvolution is uncommon in DSC-MRI, primarily since it only yields reliable results if the true residue function is well-described by the model [21].

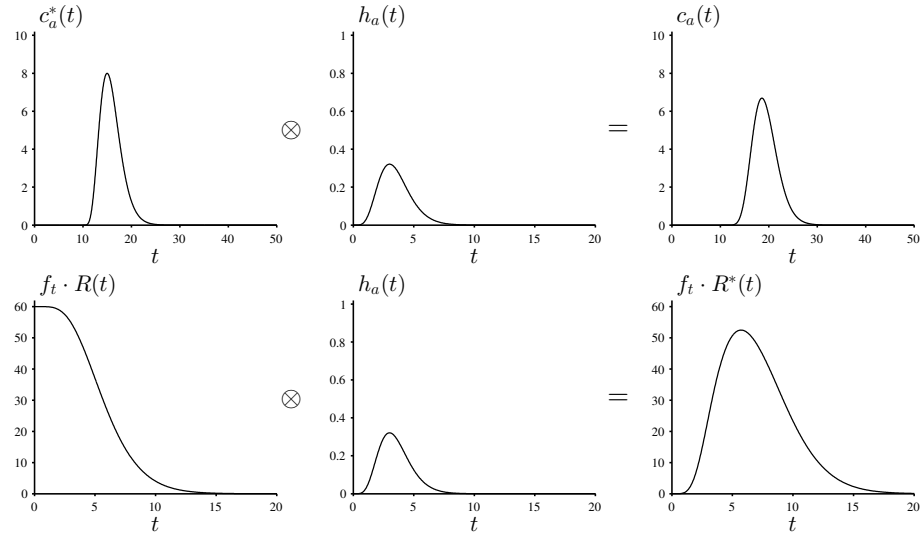

Figure 2.4: Simulated effect of dispersion on the AIF and the estimated residue function (Eq. 2.20). The top row shows the undispersed input, the vascular transport function (gamma kernel [41]), and the resulting dispersed input function. The bottom row shows the true perfusion-scaled residue function, the vascular transport function, and the dispersed residue function.

Model-free deconvolution methods can return residue functions that do not correspond to a particular functional shape. The main issue with model-free deconvolution is that it is an inverse problem, which tends to be ill-posed (no unique well-defined solution exists) and ill-conditioned (small errors in the data are amplified in the solution), and many methods are defined by the way in which they handle this issue. Transform methods are based on the convolution theorem, most commonly for the Fourier transform [20, 21, 45]. These methods are very sensitive to noise, which is usually controlled for by applying a low-pass filter that reduces high-frequency noise in the solution. Another approach for model-free deconvolution is to employ a discrete reformulation of Eq. 2.12 according to [21]

$$k_H c_t(t_j) = \rho f_t \int_0^{t_j} c_a(t) R(t-\tau) d \approx \rho f_t \, \Delta t \sum_{i=0}^{j} c_a(t_i) R(t_j - t_i), \qquad [2.21]$$

where Δt is the temporal resolution and j denotes the time-point index. By writing Eq. 2.21 in short hand $\mathbf{c_t} = \mathbf{c_a R}$ (the constants are included in the matrices), deconvolution may be performed by minimizing $\|\mathbf{c_a R} - \mathbf{c_t}\|_2^2$. As for the transform methods, this approach is very sensitive to noise, which can be controlled by minimizing the regularized problem $\|\mathbf{c_a R} - \mathbf{c_t}\|_2^2 + \gamma \|\mathbf{LR}\|_2^2$, where γ is the regularization parameter and $\mathbf{L}$ is the regularization operator. The regularization operator is usually chosen to constrain the resolved residue function to be a nonnegative, monotonically decreasing and/or smooth function of time [21, 46].

Another common way to solve Eq. 2.21 is singular value decomposition (SVD) [21].

In SVD, $\mathbf{c_a}$ is decomposed into two orthogonal matrices and a nonnegative diagonal matrix, and $\mathbf{c_a}^{-1}$ is expressed as a matrix product and used to estimate $\mathbf{R}$. A threshold on the diagonal matrix is used to truncate values so that non-physiological oscillations are suppressed in the solution (regularization). The most common deconvolution method in DSC-MRI is block-circulant SVD (cSVD), which was proposed by Wu et al. to reduce the sensitivity of SVD to delay [47]. In the same work, an adaptive thresholding approach was also proposed, called oscillation-indexed block-circulant SVD (oSVD). The SVD-based methods are characterized by low noise sensitivity and robust results, although the resolved residue functions are not necessarily nonnegative or monotonically decreasing, and may result in perfusion underestimation. Both cSVD and oSVD were used as reference methods in Paper I.

Several recent deconvolution methods are based on nonlinear fitting of Eq. 2.12 in combination with regularization, using model-free residue functions defined on a continuous time scale [36, 48, 49]. An example of this is nonlinear stochastic regularization (NSR), proposed by Zanderigo et al. [36]. This is an advanced deconvolution method which derives the shape of the residue function from a stochastic process (integral of white noise), and employs Bayesian inference for parameter estimation. Prior information about the residue function is included through the use of an exponential transform to ensure nonnegative solutions, and Tikhonov regularization to reduce oscillations. The effective residue function also includes a first order approximation of bolus dispersion (exponential), i.e., $h_a(t) = \delta^{-1}e^{-t/\delta}$, so that residue functions and perfusion values unaffected by dispersion can be estimated. As further described below, NSR was adapted to and evaluated for deconvolution in model-free ASL in Paper I.

Arterial spin labeling

ASL is a noninvasive perfusion MRI technique, proposed by Detre et al. and Williams et al. in 1992 [50, 51]. The basic idea is to magnetically label arterial blood water using radiofrequency (RF) pulses, so that the blood magnetization acts as an endogenous contrast agent. In conventional ASL, inversion pulses are applied to large arteries upstream of the tissue of interest. The labeled blood travels through the vascular tree and eventually reaches the microvascular system, were the blood water exchanges with molecules in the interstitial space. This results in a local tissue signal decrease, and the magnitude of this decrease is proportional to local tissue perfusion. By acquiring complementary control images without labeling, subtraction of the two yields a relative perfusion image known as the magnetization difference ΔM (see Figure 2.5). Since the magnetization is continuously decaying by T1 relaxation and since the blood volume is small in the brain, the effect on the signal is small and several repetitions are normally acquired to increase the signal-to-noise ratio (SNR).

The ASL contrast can be obtained in many different ways, which has resulted in

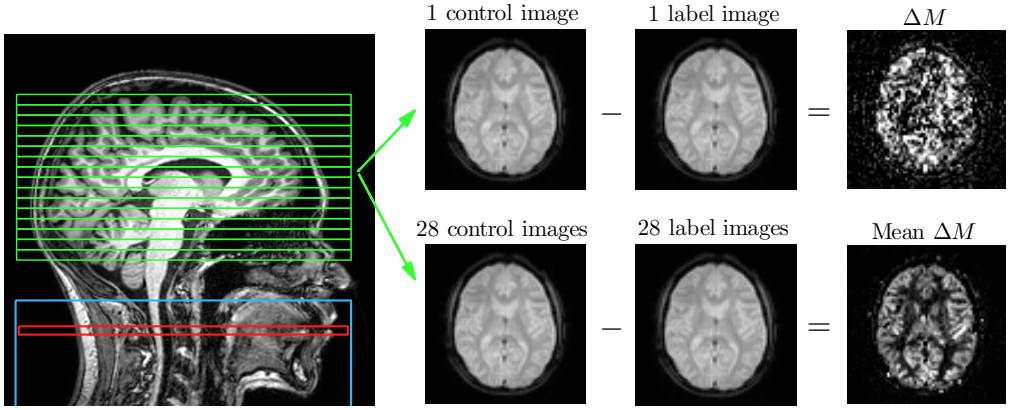

Figure 2.5: The basic concept of an ASL experiment. To the left is a standard sagittal MR image, with superimposed boxes corresponding to the imaging slices (green), PASL labeling slab (blue), and (P)CASL labeling slice (red). The three images on the top right show single control and label images, as well as the magnetization difference (ΔM) between them. It is apparent that the result is very noisy for a single ASL acquisition. The three images on the bottom right show the mean of 28 control and label images, and the corresponding mean ΔM. The result is much improved compared to the single acquisition.

an abundance of different ASL pulse sequences and methods. The different techniques are usually divided into different categories depending on the approach used for the labeling module, the most common being continuous ASL (CASL), pulsed ASL (PASL) and pseudo-continuous ASL (PCASL). In CASL, the arterial blood water is continuously labeled in a thin slice proximal to the tissue of interest [51]. A long low-power RF pulse (2–4 seconds) is applied together with a magnetic field gradient yielding a flow-driven adiabatic inversion of the spins flowing in the large arteries. This labeling type has largely been abandoned in human ASL studies, partly due to the high demand on the RF hardware. In PASL, a short RF inversion pulse (5–20 ms) is applied in a thick slab [52]. Hence, the entire bolus of labeled blood water is created instantly, which means that the amount of labeled blood is determined by the spatial extent of the inversion slab. Furthermore, compared to CASL, the labeled blood show a longer transit time on average. These issues lead to a shorter bolus, and a lower ASL signal due to T1 relaxation (Figure 2.6). PCASL can be seen as a pulsed version of CASL; it employs continuous labeling in a thin slice, although the continuous RF pulse is exchanged for a train of many short RF pulses and magnetic field gradients [53, 54]. Like CASL, the inversion is achieved through flow-driven adiabatic inversion, although PCASL has higher labeling efficiency (high SNR), a manageable load on the RF duty cycle, and less magnetization transfer effects. These advantages have led to a consensus that PCASL is the currently recommended ASL technique for clinical applications [55]. For more details on labeling types and ASL techniques, see Refs. [3, 55–57].

ASL is usually implemented as a single time-point experiment with a post-label delay (PLD; the time between end of labeling and readout) of 1.5–2 seconds to allow for most of the labeled blood to reach the tissue of interest. The bolus length is ~1.5–2

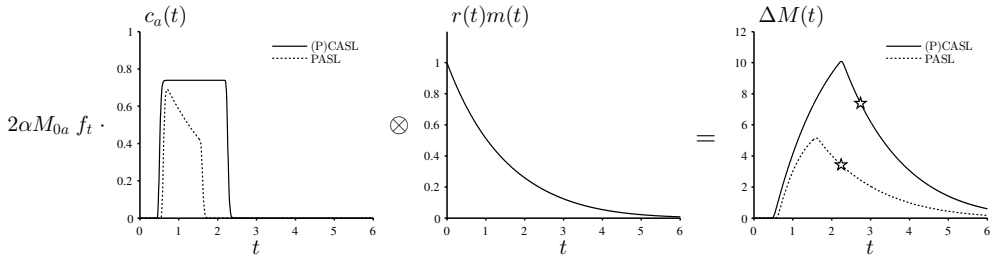

Figure 2.6: Simulation of the tracer kinetics in (P)CASL and PASL experiments using the standard model (Eq. 2.23). The left graph shows the input functions where (P)CASL yields a box-car bolus shape, whereas PASL yields a shorter bolus that decreases with the T1 of blood. The middle graph shows the combined effects of the residue function and magnetization decay by T1 relaxation. The right graph shows the resulting ASL signals. The functions start to decay after the entire bolus has been delivered, and the stars indicate approximately when imaging is performed for a single time point experiment.

seconds for PCASL and ~0.6–1 seconds for PASL. The experiment is repeated, usually until 20–40 control-label pairs have been acquired. Tissue signal suppression and crushing of macrovascular signal can be used to improve the quality of the perfusion images, and a reference PD image is usually acquired for calibration (i.e., determination of M_{0a} as described below). For multiple time-point (multi-TI) acquisitions, the post-label delay is usually varied between 0 and 4 seconds.

The general kinetic model

As mentioned in the 'Tracer kinetic modeling' section, steady-state like experiments have been used in perfusion MRI, and the original ASL implementation is an example of this. Continuous labeling was applied until steady-state was reached in the tissue of interest, and subsequent perfusion estimation was achieved using the Bloch equations modified to include the effect of the labeled blood water [50, 51]. In this context, perfusion contrast was identified as a change in the apparent T1 of tissue. Later on, it became more common to use a delay between labeling and imaging, and the PASL techniques also became more common. Therefore, the ASL analysis shifted towards a more bolus experiment oriented approach. Buxton et al. generalized this by describing ASL from the perspective of tracer kinetic modeling, which is summarized in the so-called general kinetic model for ASL [56]:

$$\begin{aligned}\Delta M(t) &= 2\alpha M_{0a}\, f_t \int_0^t c_a(t) r(t-\tau) m(t-\tau) d\tau \\ &= 2\alpha M_{0a}\, f_t \left\{ c_a(t) \otimes [r(t)\, m(t)] \right\}. \end{aligned} \qquad [2.22]$$

Here, $\Delta M(t)$ is the perfusion weighted tissue signal, $r(t)$ is the residue function, $m(t)$ is the magnetization relaxation of the labeled water, and $2\alpha M_{0a} c_a(t)$ constitutes the input function of labeled water, where α is the inversion efficiency, M_{0a} is the equilibrium magnetization of arterial blood, and $c_a(t)$ is the fractional AIF. Note the analogy with the tissue signal model in general tracer kinetics (Eq. 2.5) and DSC-MRI (Eq. 2.12). The

advantage of this general description is that it can be used to derive signal equations for many different labeling techniques and exchange models. Figure 2.6 displays a noise-free simulation of the tracer kinetics in (P)CASL and PASL experiments.

The standard model

The standard model is a simplified ASL model, based on a set of assumptions, leading to tractable ASL signal equations [56]. In short, it is assumed that labeled blood arrives at the voxel after a delay time Δt (arrival time), that the water exchange between blood and tissue is described by a well-mixed single-compartment, and that the labeled water upon arrival to the voxel starts to decay with the T1 of tissue (T_{1t}) rather than the T1 of arterial blood (T_{1a}). These assumptions can be formulated in terms of the time-dependent functions in Eq. 2.22 according to

$$\begin{aligned} c_a(t) = \; & 0 && t < \Delta t \\ & e^{-\Delta t/T_{1a}} && \Delta t < t < \Delta t + \tau \qquad [(P)CASL] \\ & e^{-t/T_{1a}} && \Delta t < t < \Delta t + \tau \qquad [PASL] \\ & 0 && t > \Delta t + \tau \\ r(t) = \; & e^{-f_t t/\lambda} \\ m(t) = \; & e^{-t/T_{1t}}, \end{aligned} \qquad [2.23]$$

where τ is the label duration[3] (length of the bolus) and λ is the brain-blood partition coefficient of water. Figure 2.6 displays these functions, together with the resulting ASL signal (Eq. 2.22). By inserting these expressions into the general kinetic model (Eq. 2.22), we obtain analytical signal equations that can be applied to single- or multi-TI ASL data. In single time-point analysis, perfusion is usually estimated by directly solving the equation for f, whereas in multi-TI analysis, the signal equation is fitted to the measured $\Delta M(t)$ curve.

By assuming that the entire bolus has been delivered to the tissue ($t - \tau > \Delta t$), that there is no outflow, and that the label only decays with T_{1a}, a very basic model for single time-point ASL is obtained according to [55]

$$\begin{aligned} \Delta M &= 2\alpha M_{0a} T_{1a} f_t \, e^{-w/T_{1a}} (1 - e^{-\tau/T_{1a}}) && [(P)CASL] \\ \Delta M &= 2\alpha M_{0a} \tau f_t \, e^{-T_I/T_{1a}} && [PASL] \end{aligned} \qquad [2.24]$$

where $w = t - \tau$ is the PLD in (P)CASL, and $T_I = t$ is the inversion time (i.e., the time between labeling and readout) in PASL. Note that many different assumptions are required to arrive at these simple and convenient signal equations, which naturally makes them prone to errors.

[3]The label duration is often denoted TI_1 in PASL experiments.

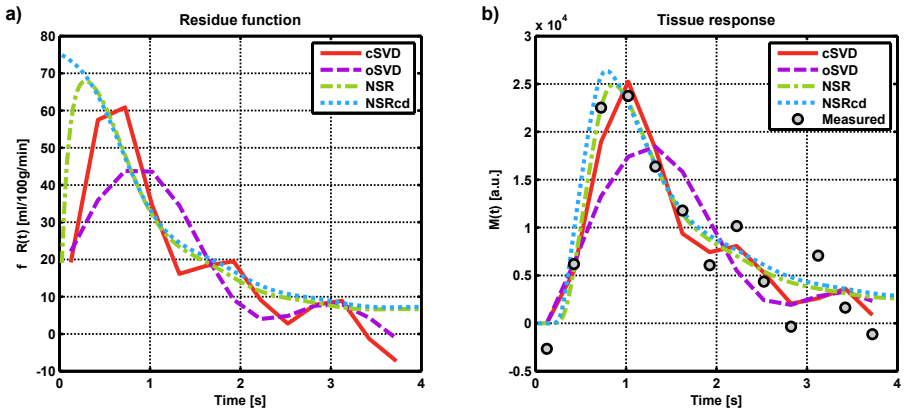

Figure 2.7: Example of deconvolution results in a single voxel, from Paper I. (a) NSR yields more reasonable residue function shapes compared to SVD, especially when correcting for dispersion (NSRcd). Heavy truncation, as for oSVD in this case, may cause severe perfusion underestimation. (b) Measured and fitted tissue signals, $\Delta M(t)$, for the different deconvolution methods. The unphysiological solutions of the SVD-based deconvolution methods are the results of overfitting, whereas NSR trades larger residuals for smoother solutions.

Model-free arterial spin labeling

Whereas Eq. 2.24 represents one of the most simplified ways to quantify perfusion with ASL, model-free ASL, devised by Petersen et al. [58], is at the other end of that spectrum. It attempts to relax and reduce the number of assumptions by employing a more advanced pulse sequence that acquires additional data, allowing for quantification by means of model-free deconvolution [58].The sequence is called QUASAR, and is designed to dynamically acquire both arterial input curves $c_a(t)$ and tissue curves $\Delta M(t)$. Similar to DSC-MRI, deconvolution of Eq. 2.22 yields the perfusion-scaled effective residue function $R_f(t) = f_t R(t) = f_t r(t) m(t)$, from which a model-free perfusion estimate is obtained. The reproducibility of model-free ASL was tested in a large test-retest study including 28 sites and 284 healthy subjects, using automatic planning to yield consistent slice positioning [59]. In an alternative approach, Chappell et al. suggested a model-based analysis of QUASAR data, including modeling of arterial dispersion [41]. The results of that study indicated the presence of substantial dispersion effects in QUASAR data.

The QUASAR sequence employs pulsed labeling and saturation recovery (SR) Look-Locker readout. The application of arterial crushers allows for estimation of $c_a(t)$ curves by subtraction of $\Delta M(t)$ with and without crushers. By identifying local AIFs with reasonable shape and SNR, voxel-wise AIFs can be calculated by appropriate scaling [60]. The SR signal evolution of the control images allows for mapping of M_{0a} and T_{1t}, which are used in the quantification. Furthermore, in Paper I, we exploited the SR data to obtain PV estimates, subsequently used to produce tissue region of interests (ROIs) and improve the M_{0a} estimation.

Due to the similarity with model-free quantification in DSC-MRI, results from model-free ASL are expected to be dependent on the applied deconvolution method, and be

sensitive to delay and dispersion. Therefore, in Paper I, we assessed the dependence of model-free ASL on the choice of deconvolution method, and the possibility to correct for delay and dispersion. Specifically, SVD-based deconvolution was used in the original model-free ASL work [58], whereas we adapted the NSR deconvolution method (described above) [36]. Even with truncation, the SVD-based deconvolution methods generates solutions with unphysiological oscillations and negative values, and the NSR deconvolution was shown to improve this also for model-free ASL. Figure 2.7 displays residue functions and signal fits for the NSR and SVD deconvolution methods. NSR with dispersion correction (NSRcd) clearly results in more physiologically plausible residue functions, i.e., monotonically decreasing nonnegative solutions.

A central motivation for this work was that truncated SVD generates can lead to perfusion underestimation [47], whereas NSR has been shown to better resolve the perfusion-scaled residue function in DSC-MRI [36]. This was verified in Paper I using simulations, and the more advanced NSR deconvolution method also yielded in vivo results in better agreement with literature perfusion values. NSR is delay sensitive, which was accounted for by employing edge detection and temporal shifting of the concentration curves prior to deconvolution. Finally, NSR includes simple dispersion modelling, and initial results suggested that NSR deconvolution can potentially correct for dispersion effects in model-free ASL. Figure 2.8 shows examples of the in vivo results from Paper I, including dependence on the applied deconvolution method, the relation between dispersion and arrival time, and PV maps. Model-free ASL was also used in Paper II, which will be further discussed in Chapter 4.

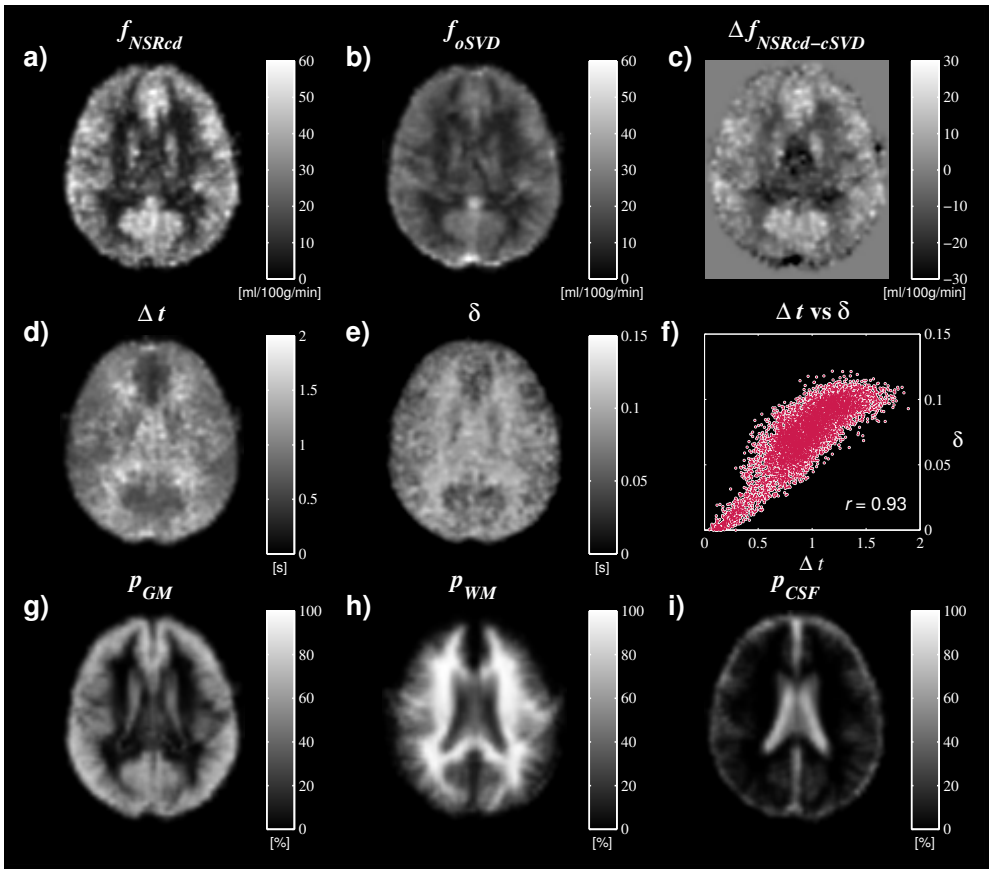

Figure 2.8: Example of group averaged (10 subjects) parameter maps in MNI space, from the model-free ASL results in Paper I. The top row shows CBF obtained with (a) NSR deconvoution, (b) SVD deconvolution and (c) the difference between the two. There is a considerable difference and, in particular, higher gray matter values are obtained with NSR. The second row shows (d) the arrival time Δt, (e) the amount of dispersion δ, and (f) the correlation between these parameters. The high correlation suggests that the dispersion modeling worked as intended, since more dispersion is expected for blood that has traveled longer. The bottom row displays PV maps for (g) gray matter, (h) white matter, and (i) cerebrospinal fluid, obtained using the SR data (see Chapter 3).

Chapter 3

Partial volume mapping

The partial volume effect (PVE) in MRI refers to the intravoxel mixing of signals from different components that occurs due to the limited spatial resolution [61]. PVE-based segmentation, or PV mapping, is a type of image segmentation in which this effect is taken into account, so that the amount of each tissue type is estimated in every voxel [62]. Since PV mapping estimates tissue volume at a sub-voxel level, it is more versatile than hard binary segmentation and can be used to improve volume metrics and quantitative MRI. For example, a PV mapping method referred to as 'fractional signal modeling' (FSM) was used in Paper I for improved M_{0a} estimation, as well as in Papers II–III for PVC of ASL and DSC-MRI data. Furthermore, a new FSM method was proposed in Paper IV. FSM is based on quantitative relaxometry, as will be described later in this chapter.

Segmentation

Image segmentation is the process of dividing an image into different segments (and sometimes to classify those segments) based on features such as intensity, pattern or other properties. Segmentation is a very broad issue which has attracted a lot of attention in digital image processing, including medical imaging and in particular MRI [63, 64]. A detailed discussion about methods and applications is outside the scope of this thesis, and we will only briefly discuss human brain segmentation. Brain segmentation often refers to automatic segmentation of a brain image into three different tissue types, i.e., gray matter (GM), white matter (WM), and cerebrospinal fluid (CSF), although the concept may also include other processes such as brain extraction (skull stripping) and segmentation of lesions/pathologies [65]. Many different segmentation methods exist, and the more robust methods are often advanced and may be difficult to implement. Fortunately, easy-to-use tools are freely available as part of standard software packages for brain image processing.

Generally speaking, segmentation is a difficult problem due to measurement noise, image artifacts, bias fields, complex anatomical structures and limited spatial resolution.

On the other hand, MRI has excellent soft tissue contrast and the main intracranial tissue types are few and generally form continuous shapes, which makes brain segmentation feasible with some work. Although this chapter is focused on automatic segmentation, it is important to note that manual delineation of ROIs is very common in clinical routine.

Most brain segmentation methods are based on the use of image intensity or quantified tissue properties. This is intuitively reasonable because many MRI sequences yield signal intensities that differ between GM, WM and CSF. The simplest intensity-based segmentation is to threshold the image, so that all voxels within a certain intensity range are assigned to a certain tissue type, but this approach generally leads to poor segmentation results. Inclusion of several different images is likely to improve the results (i.e., multi-spectral segmentation), for example, using multi-contrast or quantitative images together with predefined regions in feature space [66–69]. The advantage of using quantitative images is that the algorithm do not have to account for arbitrary and biased signal values (which can depend on hardware and protocol). Since the segmentation methods rely on tissue-specific signals, the characteristics needs to be pre-defined or estimated from the image (feature extraction).

A more advanced approach is to model the signal from each tissue type with a probability distribution (e.g., Gaussian mixture models), and to include regularization by spatial prior information to make the segmentation less noise sensitive. Thus, each voxel is assigned a probability of belonging to a certain class, based on the relative contribution of the distribution at the given intensity value, accounting for the prior information. Note that these probability values are continuous on the scale 0–1, and relate to the PVE-based segmentation methods discussed below. A traditional prior is to assume that most voxels are surrounded by voxels of the same class, which can be incorporated using Markov random field theory [70]. Another common regularization technique is to use registration to a stereotactic standard brain (spatial normalization), and subsequent segmentation using population-based priors/atlases [71]. This technique is employed within a statistical framework in the segmentation tool included in the SPM software package [72], which was used in the reference method in Paper II. Population-based atlases also allow for further parcellation of structures (i.e., to label subregions within the different tissue types, such as cortical regions and deep gray matter structures).

Many segmentation methods have been based on modelling the PVE [62]. Although simple methods exists, such as consecutively nulling different tissue types [73], most methods are rather advanced from a technical perspective (e.g., Refs. [66, 74, 75]). Most of the methods are based on a mixed model, i.e. the measured signal intensity I in a voxel is given by a weighted sum of signal intensities I_k of the different tissue types [61, 70, 74]:

$$I = \sum_k \alpha_k I_k, \qquad [3.1]$$

where $\alpha_k \in [0, 1]$ is the fraction of tissue type k. Normally, the intensities I_k (and consequently I) are assumed to be Gaussian random variables so that the problem is

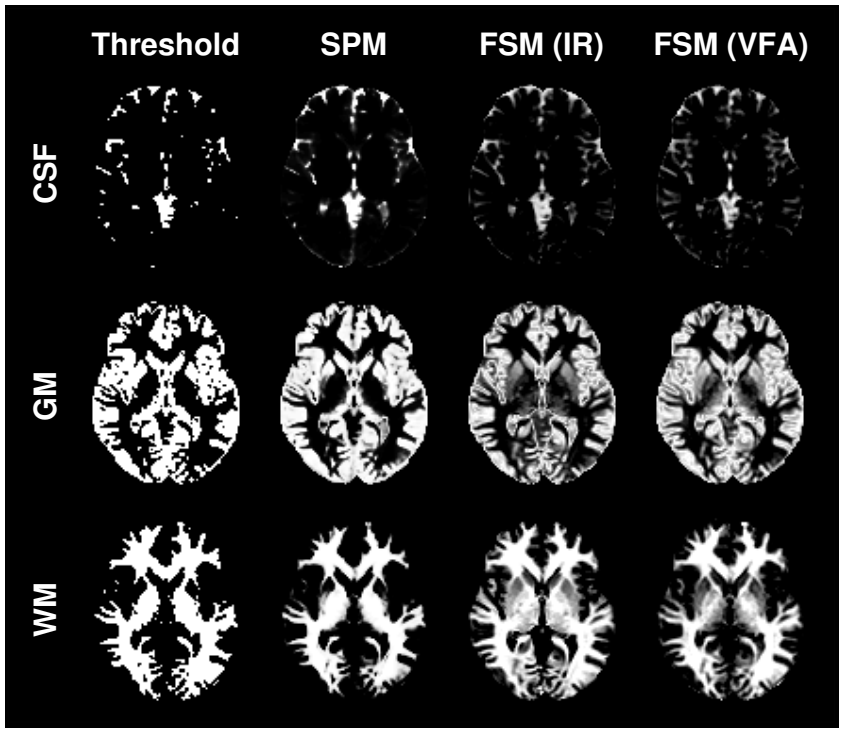

Figure 3.1: Side by side comparison of segmentation and PV mapping using, from left to right, simple thresholding, the SPM software, IR-based FSM and VFA-based FSM. The FSM methods produce more nuanced images including mixture of tissue types, whereas thresholding and the SPM software results in more traditional and binary segmentation.

tractable with statistical approaches [62]. The FSM methods discussed later can be seen as an extension of the model in Eq. 3.1, but with the individual I_k being functions of acquisition and tissue parameters, modelled according to MR signal equations.

Intensity-based segmentation is difficult, not only due to signal overlap and mixed voxels, but also due to noise and bias fields. Therefore, denoising and bias field correction is normally included in the preprocessing. In summary, most current segmentation algorithms operate in a few well-defined steps, namely pre-processing (e.g., denoising, inhomogeneity correction and skull-stripping), feature extraction, and segmentation/classification. Many more and advanced segmentation methods exist that are not discussed here, e.g. fuzzy logics, Bayesian inference and Markov random fields [63, 64].

Traditional applications of brain segmentation includes identification of ROIs for diagnosis or treatment/surgical planning, preprocessing for subsequent image processing, abnormality detection, and for regional analysis of MRI data [63]. More recent applications based on PV mapping include volumetry [76], diagnosis and prognosis of neurodegenerative diseases [77], and improvements in quantitative MRI (see Chapter 4). The FSM implementation described in Paper IV could be used in any type of application, whereas examples of FSM applications can be found in Papers I–III.

Fractional signal modeling

FSM is a new and emerging PV mapping and segmentation technique [62, 65], originally proposed by Shin et al. [78]. Only a few methodological papers exist at this point, i.e., Ref. [78] and Paper IV, but the technique has shown great potential so far (see Fig. 3.1). For example, the algorithms are robust and simple, based on conventional quantitative MRI, and have already proved valuable in perfusion MRI (see Papers I–III and Refs. [79, 80]) and fMRI [81, 82]. Although all studies so far have employed T1-based FSM, and separation of GM, WM and CSF specifically, we derive a more general framework here, applicable to different types of data and any number of tissue types (or components).

The central idea in FSM is that the observed voxel signal, as a function of one or more acquisition parameters, is modeled as a linear combination of the characteristic signal patterns expected from the different tissue types. Thus, the general FSM model can be written as

$$S(x) = \sum_i S_i(x) = \sum_i s_i \, m_i(x; \boldsymbol{\theta}_i), \qquad [3.2]$$

where $S(x)$ is the MR signal as a function of acquisition parameter x, $S_i(x)$ is the signal contribution from tissue i, s_i is the fractional signal[1] of tissue type i, and $m_i(x; \boldsymbol{\theta}_i)$ is the relative signal model (characteristic signal pattern) of tissue type i, given the tissue-specific parameters $\boldsymbol{\theta}_i$. It is straightforward to make the model multi-dimensional by including additional independent variables, e.g. $S(x, y)$ and $m_i(x, y; \boldsymbol{\theta}_i)$. A couple of things are worth noting:

- Successful PV mapping relies on that $\boldsymbol{\theta}_i$ differs between tissue types, and that variation of acquisition parameter x alters the tissue contrast.
- The models for the different tissue types need not be the same (indicated by the subscript i on the function m) but usually are.
- Tissue-specific parameters $\boldsymbol{\theta}_i$ are measured or assumed a priori (and usually fixed to single values).

If the s_i values are the only unknowns, Eq. 3.2 can be solved by means of linear least squares estimation, where the minimum number of required data points is given by the number of tissue types. Although Eq. 3.2 could be solved with different means (e.g., nonlinear least squares and statistical methods), only the linear least squares solution is described here.

The number of tissue types is denoted L with corresponding indexing variable i, and the number of measured data points is denoted N with corresponding index j. If the measured signal at discrete time points j is written as $\mathbf{S_m} = [S(x_1) \ldots S(x_N)]^{\mathrm{T}}$, we can write Eq. 3.2 in discrete matrix form according to

$$\mathbf{S_m} = \mathbf{X}\mathbf{s} + \boldsymbol{\epsilon}, \qquad [3.3]$$

[1]The fractional signal $s_i \in [0, M_0]$ can be interpreted as the contribution of tissue i to the voxel equilibrium magnetization M_0.

where $X_{ji} = m_i(x_j; \boldsymbol{\theta}_i)$, $\mathbf{s} = [s_1 \dots s_L]^{\mathrm{T}}$ and $\boldsymbol{\epsilon}$ is a $N \times 1$ noise vector. Now, Eq. 3.3 can be solved for $\mathbf{s}$ with linear least squares estimation. Since s_i values are nonnegative and sum up to M_0, the estimation can benefit from using constrained least squares, i.e., minimization of $\|\mathbf{X}\mathbf{s} - \mathbf{S_m}\|_2^2$ subject to $\mathbf{s} \geq 0$ and/or $\sum_i s_i = M_0$.

PV estimates in units of relative voxel volume, $p_i \in [0, 1]$, can be obtained from the fractional signal estimates by accounting for tissue-specific water densities ρ_i and normalizing:

$$p_i = \frac{s_i/\rho_i}{\sum_i s_i/\rho_i}. \qquad [3.4]$$

An interesting feature of FSM is that, as long as unique characteristic tissue signals can be reasonably established, the PV estimates do not depend on quantitative values for $\boldsymbol{\theta}_i$, and they are insensitive to spatially varying scaling factors such as $B1^-$. However, any spatial variation of the true characteristic curves (e.g., due to spatial variations in $\boldsymbol{\theta}_i$ or $B1^+$) will lead to errors unless accounted for. This leads us to one of the most crucial parts of FSM, namely how to determine the $\boldsymbol{\theta}_i$ values.

For T1-based FSM, a few different ways to set the tissue specific T1 values (T_{1i}) have been suggested. The most simple approach is to use fixed literature values [81]. However, this approach is highly sensitive to inter-subject variations and, therefore, Shin et al. suggested to estimate T_{1i} values subject-wise by employing standard T1 mapping and subsequent analysis of the whole-brain histogram, as a pre-processing step (see Figure 3.2 and Ref. [78]). However, due to the small CSF volume, literature values are often used for CSF (one exception being Paper IV in which CSF T1 was estimated from a ventricle region). In a low-resolution application, Petr et al. argued that the resolution was too low to allow for estimation of GM T1 from the histogram analysis, and instead adopted a least squares iterative estimation [79]. Even if T_{1i} values are estimated on a subject basis, the within-tissue T_{1i} values are fixed, which corresponds to an assumption that representative values exists for each tissue type. To relax this assumption, Oliver suggested to let GM T1 vary spatially (regularizing the problem by constraining the value to be fixed in a local region), which improved classification of deep GM structures [80]. Further investigation and development of the handling of $\boldsymbol{\theta}_i$ in FSM analysis is needed, which could include assessment of spatial priors and statistical approaches.

We want to stress the impressive robustness, in relation to its simplicity, that FSM exhibits. While most segmentation methods discussed above require many different processing steps, and are very complex and difficult to implement (which leads to higher demand on expertise and less accessible code [72]), the FSM technique is, in its basic form, very simple. For example, FSM can be implemented with just one extra processing step added to a standard T1 quantification script. Although multiple acquisitions are required, the data can be acquired with conventional and widely available pulse sequences. Another advantage is that FSM is, to a large extent, independent on hardware and protocol settings and does not rely on predefined tissue maps or features, which makes it applicable to a wider range of individuals such as different ages and patient groups [78].

Inversion and saturation recovery acquisition

The most common method to date has been T1-based FSM, in particular using inversion recovery (IR) and SR data. Assuming that the repetition time $T_R \gg T_1$ and disregarding T2-weighting, the signal equation for a standard IR or SR sequence is given by $S(t) = M_0(1 - Ae^{-t/T_1})$, where M_0 is the equilibrium magnetization, and $A = (1 - \cos\theta)$, where θ is the flip angle of the preparation pulse. Thus, $A = 2$ for an ideal inversion and $A = 1$ for an ideal saturation, and t is usually denoted T_I and T_S for IR and SR, respectively. By using the standard signal equation as a basis for $m_i(x; \boldsymbol{\theta}_i)$, the IR/SR-based FSM model becomes

$$S(t) = \sum_i s_i \, m(t; T_{1i}) = \sum_i s_i \, (1 - Ae^{-t/T_{1i}}), \qquad [3.5]$$

where T_{1i} is the T1 of tissue i. Note that M_0 is included in the s_i values rather than $m(t; T_{1i})$. As an example of FSM analysis, a post-processing pipeline for SR-based FSM is summarized graphically in Figure 3.2. In contrast to many signal intensity based segmentation algorithms, the widths of the different peaks in the histogram are not used here.

In the original paper, Shin et al. used a special IR sequence with Look-Locker EPI readout in steady-state, and called that FSM implementation 'fractional signal mapping from inversion recovery' (FRASIER) [78]. The Look-Locker readout employs a train of low flip angles to rapidly acquire images at different times t. This results in a steady state magnetization given by

$$M_0^* = M_0 \, \frac{1 - e^{-\Delta T/T_1}}{1 - \cos\phi \cdot e^{-\Delta T/T_1}}, \qquad [3.6]$$

and a corresponding apparent longitudinal relaxation time given by

$$\frac{1}{T_1^*} = \frac{1}{T_1} - \frac{\ln(\cos\phi)}{\Delta T}, \qquad [3.7]$$

where ΔT is the time between successive RF pulses, and ϕ is the flip angle of those pulses. If the inversion pulse is applied at steady state, and including the effects of the Look-Locker readout, the signal recovery follows $S(t) = M_0^*(1 - Ae^{-t/T_1^*})$, and the corresponding FSM model becomes [78]

$$S(t) = \sum_i s_i \, \frac{1 - e^{-\Delta T/T_{1i}}}{1 - \cos\phi \cdot e^{-\Delta T/T_{1i}}} \, (1 - Ae^{-t/T_{1i}^*}), \qquad [3.8]$$

which can be solved by linear least squares estimation as described above.

This implementation of FSM was proposed in [78], and was employed in Papers I–III and Refs. [79–82]. In Paper II, simulations suggested good performance of FSM applied to native low-resolution ASL data. It should be noted that Shin et al. assumed ideal inversion preparation ($A = 2$) and excitation pulses [78], whereas we accounted for non-ideal saturation preparation and spatial variation of ϕ in Papers I–II.

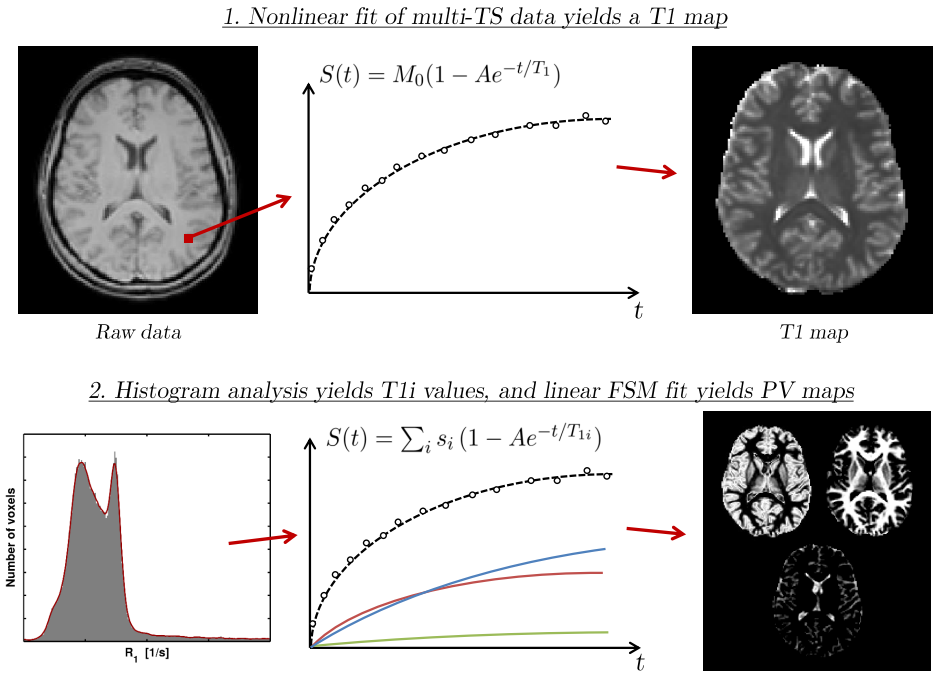

Figure 3.2: The FSM concept exemplified with an SR-based approach. The top row displays a conventional voxel-wise signal equation fit producing a T1 map. The bottom row describes how T1 histogram analysis is used to estimate tissue-specific T1 values, and how subsequent FSM analysis yields PV maps. The example voxel FSM fit yielded an estimated mixture of GM and WM (blue and red lines), and very little CSF (green line).

Variable flip angle acquisition

This is an alternative T1-based FSM method, originally described in Paper IV. In this work, we suggested to adapt FSM to the conventional T1 mapping by variable flip angle (VFA) technique [83, 84]. Omitting T2*-weighting, the signal equation for a spoiled gradient-recalled echo (SPGR) as a function of flip angle θ is given by

$$S(\theta) = M_0 \sin\theta \frac{1 - e^{-T_R/T_1}}{1 - \cos\theta \cdot e^{-T_R/T_1}}, \qquad [3.9]$$

and the corresponding VFA-based FSM model becomes

$$S(\theta) = \sum_i s_i\, m(\theta; T_{1i}) = \sin\theta \sum_i s_i \frac{1 - e^{-T_R/T_{1i}}}{1 - \cos\theta \cdot e^{-T_R/T_{1i}}}, \qquad [3.10]$$

Since the flip angle is the independent variable, this approach is very sensitive to $B1^+$ variations and, therefore, local flip angle variations should be considered. In Paper IV, we successfully demonstrated the feasibility of this approach, dubbed SPGR-SEG, using a 3D SPGR sequence and local flip angle correction. In vivo PV maps were of good quality, and in

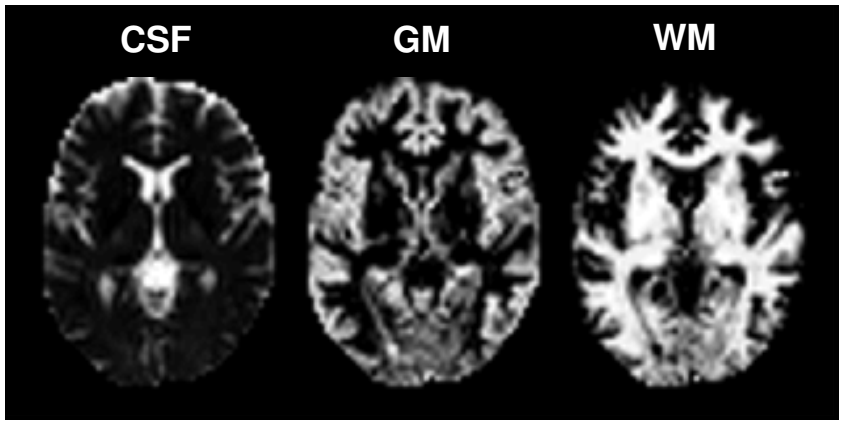

Figure 3.3: Example of T2-based FSM results achieved using T2-preparation (unpublished data). The T2 contrast between GM and WM is smaller than the corresponding T1 contrast, but T2-based FSM still seems feasible.

good agreement with IR-based FSM (Figure 3.1). Simulations suggested good performance at reasonable SNR levels, and indicated that separation of a fourth component (e.g., a lesion) would be challenging with the current protocol.

Note that different types of linearizations of Eq. 3.9 exist, which could be used for faster T1 mapping and be incorporated in the FSM model. However, such transforms leads to a non-symmetric noise distribution which makes the fitting less straight-forward.

Variable T2 weighting

By acquiring images with different T2 weightings (e.g., different echo times or T2-preparation), T2-based FSM can be achieved. For a standard spin or gradient multi-echo acquisition, $S(T_E) = M_0 e^{-T_E/T_2^{(*)}}$, and the T2-based FSM model becomes

$$S(T_E) = \sum_i s_i \, m_i(T_E; T_{2i}^{(*)}) = \sum_i s_i \, e^{-T_E/T_{2i}^{(*)}}, \qquad [3.11]$$

In a preliminary study, low-resolution T2-based FSM by variable T2-preparation yielded reasonable results (see Figure 3.3).

Other contrasts and multi-dimensional acquisition

Any variable weighting that yields sufficient contrast between different tissue types can, in theory, be used for FSM-based PV mapping and segmentation. In addition to T1- and T2-weighting, magnetization transfer contrast might be a potential contender. As for conventional segmentation approaches, FSM is likely to benefit from employment of a multi-spectral approach, for example, combining variable T1- and T2-weighting.

This could potentially enable separation of more components or improve segmentation of challenging structures such as deep GM.

Diffusion MRI has a long history of multi-component modeling approaches similar to FSM, although these have often been focused on improving diffusion metrics rather than estimating volumes. Although CSF-to-parenchyma contrast is high in diffusion MRI, it is difficult to separate GM and WM based solely on the diffusion coefficient. However, diffusion contrast can differ between other components, and this has been exploited using, for example, bi-exponential fitting with low b-values to separate blood and tissue (see Chapter 5), bi-exponential fitting using high b-values to separate fast and slow diffusion compartments [85], or fitting of multiple tensor models to separate intra-cellular, extra-cellular and free water [86, 87].

Chapter 4

Partial volume correction in perfusion MRI

The partial volume effect

As described in the previous chapter, PVEs occur due to the limited spatial resolution relative to the size of the features that are being imaged. Hence, the signal does not only depend on the experimental settings and the intrinsic properties of a given tissue, but also on the relative contribution of each tissue type to the mixed voxel signal [61]. For example, in nuclear medicine, the effective spatial resolution is determined by a combination of the voxel size and the point spread function [88]. The corresponding PVEs are known as the sampling effect and spill-in/spill-out effects, respectively. In MRI, on the other hand, the spatial resolution is often determined exclusively by the voxel size, because the point spread function is often smaller than the voxel size [61]. This means that we usually do not have to consider signal components originating from neighboring voxels influencing the voxel of interest (one exception being readout modules that yields substantial spatial blurring). In general, functional imaging techniques tend to employ lower resolution than morphological imaging, leading to more severe PVEs. For example, PVEs impede the interpretation of brain perfusion MRI, especially in thin cortical GM. Errors in tissue perfusion estimates can thus occur due to a mixture of GM and WM perfusion signals, or due to contamination with non-perfused tissue such as CSF.

Arterial spin labeling

Due to the limited SNR, ASL experiments include repeated data collection with low spatial resolution, of which the latter results in considerable PVEs (see Fig. 4.1). The mixed ASL signal can be modelled according to [89, 90]

$$\Delta M = \sum_i p_i \Delta M_i = p_{GM}\Delta M_{GM} + p_{WM}\Delta M_{WM} + p_{CSF}\Delta M_{CSF} + p_a \Delta M_a, \quad [4.1]$$

where p_i represents the PV values and ΔM_i is the magnetization difference of tissue i (which can be modeled as a function of time for multi-TI applications [90]). Note that ΔM_{CSF} is usually set to zero, and most studies also omit the arterial blood signal contribution ($p_a \Delta M_a$), which is valid if the arterial blood signal is negligible or properly crushed. In the original ASL PVC paper, Asllani et al. also included tissue-specific equilibrium magnetizations (M_{0i}) in the PVE model [89], whereas most subsequent studies have settled with only estimating ΔM_i, which has the benefit of simplifying the post-processing.

The PVE for the voxel perfusion can in turn also be modeled as a weighted sum according to

$$f_t = \sum_i p_i \frac{\Delta M_i}{M_{0a}} G_i = \sum_i p_i f_i, \qquad [4.2]$$

where G_i includes the factors needed to convert $\Delta M_i / M_{0a}$ to perfusion values f_i (i.e., the remaining part of the ASL model, including tissue-specific and acquisition parameters). This model is convenient since it is immediately seen that if, for example, the arterial blood is not crushed and not accounted for, tissue perfusion will be overestimated in proportion to the partial volume of arterial blood. If we set ΔM_{CSF} and ΔM_a to zero, and assume that $G_{GM} = G_{WM}$, a simplified PVE perfusion model is obtained according to

$$f_t = p_{GM} f_{GM} + p_{WM} f_{WM}. \qquad [4.3]$$

This simplification was used in Papers II–III.

Dynamic susceptibility contrast MRI

All previous PVC studies in perfusion MRI have been focused on ASL. Although DSC-MRI generally employ higher resolution than ASL, PVEs could still be a source of error in tissue-specific perfusion estimation. Therefore, in Paper III, we wanted to assess the PVEs and the possibility to perform PVC in DSC-MRI. The mixed DSC-MRI signal can be written as (cf. Eq. 2.10)

$$\begin{aligned} S(t) = \sum_i p_i S_i(t) &= S_0 \sum_i p_i \, e^{-T_E [R_{2i} + \Delta R^*_{2i}(t)]} \\ &= S_0 \sum_i p_i \, e^{-T_E [R_{2i} + r^*_{2i} c_i(t)]}, \end{aligned} \qquad [4.4]$$

where subscript i denotes tissue-specific quantities. This model could potentially be fitted to the data as is, although we opted for a simpler approach in the form of a post-hoc PVC, based on a simplified PVE model.

First, we assumed that r^*_2 is equal in GM and WM, as predicted by simulations [26]. By factoring out the native relaxation rates R_{2i}, and acknowledging that $c_{CSF}(t) = 0$,

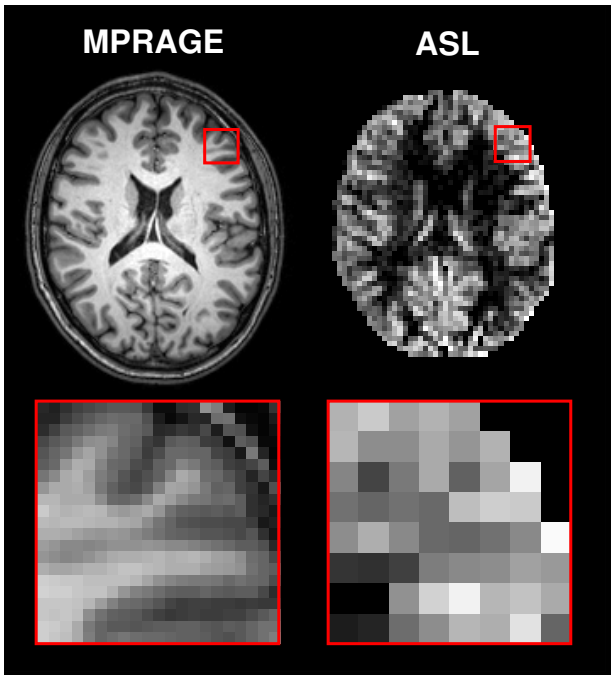

Figure 4.1: PVE examples for different spatial resolutions. The same slice of the same subject is shown for a high-resolution anatomical image (left) and a low-resolution ASL perfusion map (right). The panels at the bottom display zoomed parts (red box). The limited resolution of the ASL data results in an abundance of mixed voxels, which results in severe PVEs in the perfusion image. Adapted from Ref. [80].

combining Eqs. 2.10 and 4.4 yields

$$e^{-T_E r_2^* c(t)} = p_{GM} e^{-T_E r_2^* c_{GM}(t)} + p_{WM} e^{-T_E r_2^* c_{WM}(t)} + p_{CSF}. \qquad [4.5]$$

Using a first-order Taylor expansion, we obtain

$$\begin{aligned} 1 - T_E r_2^* c(t) &\approx p_{GM}[1 - T_E r_2^* c_{GM}(t)] + p_{WM}[1 - T_E r_2^* c_{WM}(t)] + p_{CSF} \\ \Leftrightarrow \quad c(t) &\approx p_{GM} c_{WM}(t) + p_{GM} c_{WM}(t), \end{aligned} \qquad [4.6]$$

where we have used the fact that $\sum_i p_i = 1$. This constitutes a linear approximation of the mixed tissue tracer concentration. By further assuming similar temporal tracer kinetic patterns in GM and WM, and use that $c(t) \propto f$, we end up with the same simplified mixed perfusion model as for ASL, i.e., $f_t = p_{GM} f_{GM} + p_{WM} f_{WM}$ (Eq. 4.3). It should be emphasized that several assumptions had to be made, and potential errors associated with this simplified model were therefore assessed. In particular, it was found that the linear approximation and different R_{2i} values lead to the largest uncertainties (in terms of bias), whereas the assumption of similar tracer kinetic patterns in GM and WM yielded negligible errors. Note that these simulations only considered the PVE model, i.e., not how the uncertainties propagate into PV corrected perfusion estimates.

Partial volume correction

As seen above, uncorrected perfusion values actually reflect a combination of underlying tissue perfusion and local tissue volume. Depending on the clinical question, it can be of considerable importance to separate these two quantities. This is especially true for the study of conditions in which a volumetric tissue alteration is plausible, for example, cerebral atrophy in the elderly or in connection with neurodegenerative diseases [91, 92]. Furthermore, PVC could potentially reduce the inter- and intra-subject variation of perfusion values since it reduces variability originating from tissue volume and PVEs. For example, it has been reported that ASL-based fMRI is improved when PVC is applied [93]. PVC might also improve perfusion estimation when using readout modules with non-negligible spatial blurring [80].

Partial volume correction methods

Several ways to correct for PVEs, i.e., PVC methods, have been proposed in the literature, for example in nuclear medicine [88, 94, 95] and volumetric MRI [61, 70, 74]. For PVC in perfusion MRI, the following methods are available:

- **Rescaling with a fixed tissue perfusion ratio:** This is a simple and straight-forward correction, suggested for PVC of ASL by Johnson et al. [96]. It is based on an assumed global GM-to-WM perfusion ratio, e.g., $r = f_{GM}/f_{WM} = 2.5$. This means that if the voxel perfusion and partial volumes are known, PV corrected tissue perfusion values can be estimated according to $f_{GM} = f_t/(p_{GM} + p_{WM}/r)$ and $f_{WM} = f_t/(p_{GM}r + p_{WM})$.

- **Linear regression (LR):** With this method, ΔM_{GM} and ΔM_{WM} are estimated using a local LR approach, as proposed by Asllani et al. [89]. This means that tissue signals ΔM_i are assumed to be constant in a $n \times n \times 1$ region around each voxel, which stabilizes the otherwise underdetermined problem. In practice, we first write Eq. 4.1 in matrix form according to $\Delta M = \mathbf{P}\,\delta\mathbf{m}$, where $\delta\mathbf{m}$ contains the ΔM_i and $\mathbf{P}$ contains the partial volumes p_i. Adding the local constraint by assuming that $\delta\mathbf{m} = \delta\bar{\mathbf{m}}$ over a $n \times n \times 1$ regression kernel, the problem can be formulated as $\Delta\mathbf{M_m} = \mathbf{P}\,\delta\bar{\mathbf{m}} + \boldsymbol{\epsilon}$, where $\Delta\mathbf{M_m}$ is a column vector containing all measured difference signals in the kernel, $\mathbf{P}$ is a $n^2 \times 3$ matrix formed by stacking the p_i values in the kernel, $\delta\bar{\mathbf{m}}$ is a column vector with the tissue-specific magnetization differences, and $\boldsymbol{\epsilon}$ is a noise column vector. This equation can be solved for $\delta\bar{\mathbf{m}}$ by means of linear least squares estimation, and tissue-specific perfusion values can then be calculated using conventional ASL models. The local consistency assumption introduces a spatially varying smoothing of the resulting f_i maps (larger kernels results in more pronounced smoothing) and all methods listed below aim to reduce this smoothing effect.

- **Bayesian inference:** This PVC approach was originally proposed by Chappell et al. for multiple time-point ASL data [90]. They modeled $\Delta M(t)$ as a weighted sum of the individual kinetic tissue signals (including the macrovascular component), which in turn were based on standard ASL models. The Bayesian inference was based on a Markov random field including several parameter priors, as well as adaptive spatial priors on f_{GM} and f_{WM}, meaning that the amount of smoothing is inferred from the data and can vary across the brain. The adaptive spatial priors were implemented specifically to minimize the smoothing effect inherent to the LR method.

- **Modified least trimmed squares (mLTS):** This method, proposed by Liang et al [97], is similar to LR but uses iterative ranking of residuals and matrix trimming. For an $n \times n$ kernel, an initial subset is built by successively adding ΔM values that are close to the central kernel value, until rank 2 is reached. Initial ΔM_i estimates are then obtained by standard LR on that subset. Next, the residuals are calculated and sorted, and the $n \times n \times \alpha$ voxels with smallest residuals are used to form a new subset, where α is the trimming factor. The estimation, ranking and trimming is then repeated a fixed number of times, and the final ΔM_i estimates are used to calculate f_i values. As with the Bayesian approach, mLTS has been shown to yield a lower degree of smoothing compared to LR.

- **Expectation maximization and linear regression (EM-LR):** Liu et al. suggested a PVC method exploiting temporal information in terms of the repeated acquisitions in ASL [98]. A statistical model is used so that each single ΔM (from the repeated acquisition) is considered to be an observation of a random Gaussian variable for which the mean and standard deviation are parameters to be estimated. Since the sum of two Gaussian variables is Gaussian, the problem can be solved numerically with a conventional EM estimation. Spatial information was indirectly incorporated by using the LR method on each measured ΔM for calculation of voxel-wise initial parameter estimates, which yielded better results and faster convergence compared to EM with fixed initial estimates. Note that no regression kernel is used for the EM estimation.

- **Weighted ridge regression (WRR):** To reduce the smoothing effect of LR, a smaller kernel can be used. However, this reduces the amount of available data leading to rank deficiency and high sensitivity to noise. In ridge regression, this is circumvented by introducing a bias in the estimator, i.e., trading some bias for a reduction in variance. In weighted regression, different data points are given different weights, usually to account for outliers and variable uncertainty in data. The weights can be predetermined (e.g., a Gaussian function) or estimated from the data (e.g., robust regression). Weighted ridge regression (WRR) combines the two, and the biased and weighted estimator can be formulated as $\hat{\beta}_{WRR} = (\mathbf{X}^{\mathrm{T}}\mathbf{W}\mathbf{X} + \lambda\mathbf{I})^{-1}\mathbf{X}^{\mathrm{T}}\mathbf{W}\mathbf{Y}$, where $\mathbf{X}$ is the design matrix, $\mathbf{W}$ is a diagonal matrix containing the weights, λ is

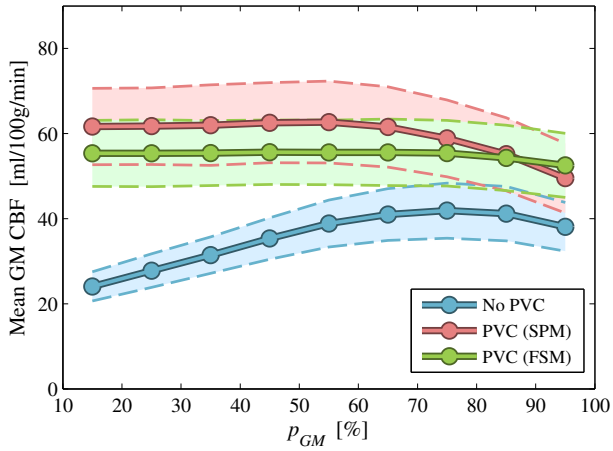

Figure 4.2: Consistency graph of GM perfusion versus GM volume in ten healthy subjects scanned four times each, from the results in Paper II. The x-axis corresponds to different 10% intervals of GM PVs (10–20%,..., 90–100%), and the different curves correspond to uncorrected perfusion values (blue), intrinsic GM perfusion values using PV estimates from SPM segmentation of an MPRAGE image (red), and intrinsic GM perfusion values using FSM-based PV estimates from the ASL raw data. The curves correspond to mean values across all 40 scans, and $\pm$ one standard deviation is shown as dashed lines enclosing colored fields.

the regularization parameter, $\mathbf{I}$ is the identity matrix and $\mathbf{Y}$ is the measured data points. Determination of λ is delicate, and two main approaches can be identified: (1) λ can be determined before the analysis, so that it works like a prior, or (2) λ can be calculated from the data, which corresponds to no prior information but an adaptive amount of regularization. Figure 4.3 displays initial results with this method (unpublished data).

The above methods can be used with Eq. 4.1 or Eq. 4.3, and although these methods where suggested for PVC in ASL, the concepts are not limited to that technique. In Paper III, for example, we applied both LR and mLTS to DSC-MRI. Modifications and extensions to some of these methods have been suggested, for example, Chappell et al. [90] and Petr et al. [79] applied LR to multi-TI data, Oliver performed PVC with a 3D kernel and adapted the Bayesian approach to single-TI data [80], and in the current thesis projects, circular instead of square kernels were employed (Papers II–III). Furthermore, acquisition of PV estimates using FSM in native space has been shown to improve PVC in ASL (see Ref. [79] and Paper II).

Method evaluation, comparison and consistency assessment

It is important to evaluate any new PVC method, and to assess the results of PVC applied to a specific subject. Evaluation of PVC methods has mostly been done using simulations, e.g., assessing the performance in terms of accuracy [90]. Simulation of hypo- and hyperintensities has also been used to demonstrate the improved preservation of

boundaries of the Bayesian, mLTS and EM-LR methods, as compared to LR [90, 97, 98].

It is difficult to assess a PVC method applied to in vivo data since no ground truth is available and, therefore, many researchers have used a reference PVC method or setting for comparison. For example, a good kernel size or preferred PV mapping technique can be informed by root mean square deviation of the PVC regression [79, 89], and the amount of smoothing can be compared with a reference method using an image gradient score [80]. Most PVC studies display the consistency of mean tissue perfusion values across different intervals of tissue volume, as shown in Figure 4.2. This is a compact and intuitive way to demonstrate the dependence of the perfusion estimates on tissue volume. In Paper II it was found that PV mapping based on native space ASL data improved the consistency compared to segmentation of a high-resolution anatomical image (Fig. 4.2), in agreement with Ref. [79]. This type of plot was also used in Paper III, where it was found that PVC based on LR showed a higher consistency than mLTS. Note that, due to the smoothing effect of some PVC methods, and since the true underlying perfusion is not necessarily independent on PV values, a straight line cannot unequivocally be regarded as the ground truth.

Similar to how Shin et al. evaluated IR-based FSM [78], Kuijer et al. suggested to validate PVC results by artificially lowering the spatial resolution through downsampling and smoothing of both PV and perfusion data [99]. The idea here is that, if the PVC works as intended, tissue-specific perfusion estimates should not be altered upon downsampling or smoothing. The authors found that, while simulated data passed this consistency check, in vivo data did not (downsampling and smoothing increased GM perfusion estimates). Whereas the reason for this failure was unclear, it did not seem to be due to spatial mismatch or a non-ideal point spread functions, which is in agreement with another study on the robustness of PVC in ASL with respect to mismatch and resolution issues [100].

Interpreting partial volume corrected perfusion

Figure 4.3 displays examples of parameter maps obtained from an ASL PVC analysis. Some variety can be found in the reporting of PV corrected perfusion estimates, for example, tissue-specific perfusion values have been reported both in terms of partial tissue perfusion values $p_i f_i$, and in terms of intrinsic tissue perfusion values f_i. The two definitions originate from two different ways of acknowledging PVEs.

The former approach views PVC as a way to separate the perfusion contribution from different components. This has a strong connection to nuclear medicine where the total number of counts or the total radioactivity for a specific tissue type or region is of interest. In the case of perfusion MRI, this approach can be used if estimation of the total blood delivery to a specific tissue type is of interest. Note that $p_i f_i$ values can be misleading since they do not reflect the underlying perfusion, but rather the contribution to the voxel perfusion estimate originating from tissue i.

The latter approach acknowledges that the PVEs perturb the estimation of tissue

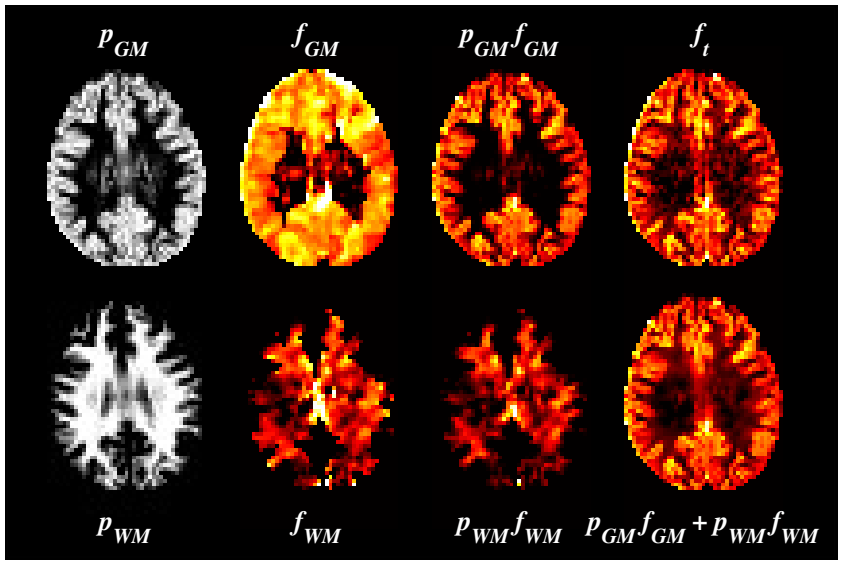

Figure 4.3: Example of parameter maps from an ASL PVC analysis. PV estimates p_i are shown in the left-hand column, intrinsic tissue perfusion values f_i in the second column (unmasked), and partial tissue perfusion values $p_i f_i$ in the third. The column to the far right displays the measured perfusion (top) and the recombined voxel perfusion using the PVC results (bottom). In this particular case, PCASL with 2D EPI readout was employed, PV estimates were acquired with SR data and T1-based FSM using the same readout as the ASL sequence, and PVC was achieved by WRR with a 3×3 kernel, Gaussian weights ($\sigma^2 = 1$ voxel), and $\lambda = 0.01$.

perfusion in volume- or mass-specific units. This approach should be used if one wants to separate the effects of tissue perfusion and tissue volume. It should be noted that the f_i maps tend to look unnatural, since much of the morphological information has been removed. Yet another quantity is the recombined voxel perfusion, i.e., $p_{GM}f_{GM} + p_{WM}f_{WM}$, corresponding to a filtered version of the measured perfusion map, which reintroduces the PVEs. The recombined map can be compared with the measured perfusion map as a simplistic assessment of the quality of the PVC fit.

Chapter 5

Incoherent flow imaging

Intravoxel incoherent motion

In 1986, Le Bihan et al. introduced the term IVIM to highlight that diffusion-sensitized MRI is sensitive to many different types of motion, i.e., not only molecular diffusion [101][1]. For example, diffusion MRI signals can include effects of motions such as flow of blood or other fluids. This eventually led to the concept of separating and quantifying diffusion and perfusion, based on diffusion MRI data [102]. Since then, IVIM imaging has been known as a method for probing perfusion using the contamination from microvascular blood flow in diffusion MRI. By making certain assumptions about the capillary network, perfusion parameters obtained from the IVIM concept may be linked to traditional perfusion parameters such as blood volume and blood flow [103–105]. Hence, IVIM imaging has been suggested as a potential way to measure blood volume noninvasively, and the clinical potential is high [106, 107]. However, widespread use of the technique has, particularly in brain applications, been prevented by the fact that the analysis demands high SNR [108, 109], and the validity the method and and interpretation of the parameters is still under debate [110].

Theory

In contrast to the perfusion MRI techniques previously discussed, IVIM imaging does not rely on tracer kinetic modeling, but on spin dephasing. Spins with varying velocity vectors (amplitude and/or direction) lead to phase dispersion when a diffusion-encoded sequence is employed. This dephasing manifests as a signal attenuation, which can be modelled depending on the type of motion. In the simplest IVIM approach, the measured signal

[1]This article actually presented the first human in vivo diffusion MRI results (excluding conference abstracts), and it also introduced the well-known b-value and apparent diffusion coefficient (ADC) notations. The term ADC was proposed in particular to highlight that in vivo diffusion measurements are sensitive to all types of IVIMs.

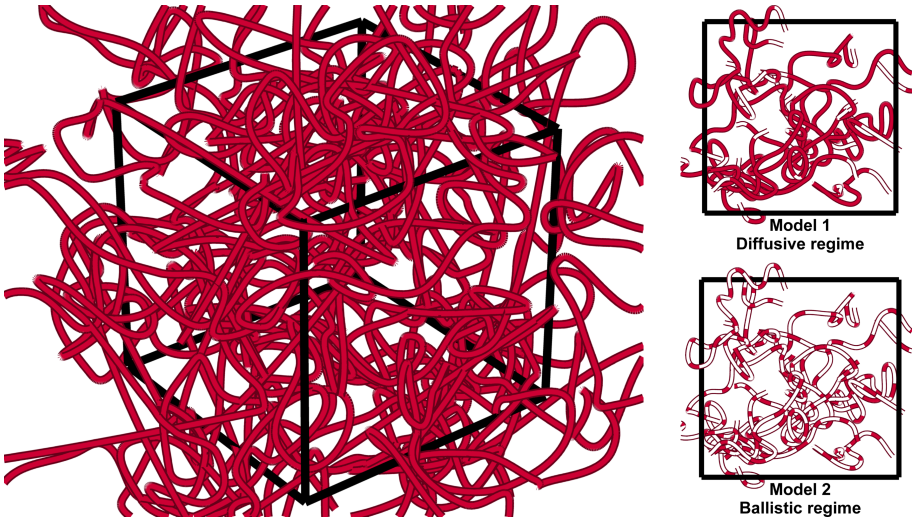

Figure 5.1: Schematic figure (not to scale) of the intricate network of highly tortuous and pseudorandomly oriented microvessels in a voxel (left). The fractional microvascular volume is on the order of a few percent in the brain. The two figures on the right visualize the two most common models for incoherent blood flow dephasing. In these figures, the red filling in the vessels corresponds to the pathway that a certain blood particle has traveled during the motion-encoding period. For the diffusive regime (model 1), the blood particles travels relatively long distances and passes several bends of the capillaries. In contrast, for the ballistic regime (model 2), the blood particles travels only a short distance and in a mostly straight path.

is modelled as a weighted sum of signal contributions from two components, i.e., (1) static tissue exhibiting molecular diffusion, and (2) blood water flowing through the capillary system [102]:

$$S(b) = S_0 \left[(1-f)e^{-bD_t} + fe^{-bD^*} \right], \qquad [5.1]$$

where b is the diffusion weighting factor (b-value) reflecting the degree of diffusion encoding, S_0 is the signal for $b = 0$, f is the normalized fractional signal of water flowing in perfused capillaries ('perfusion fraction'), $(1-f)$ is the normalized fractional signal of static tissue ('tissue fraction'), D_t is the diffusion coefficient in tissue, and D^* is the pseudodiffusion coefficient, i.e., the apparent diffusion coefficient of blood, including effects of microvascular flow. Note that the perfusion attenuation factor, $F = e^{-bD^*}$, has the same functional form as the attenuation factor due to diffusion.

The b-value is given by

$$b = \int_0^{T_E} q(t)^2 dt, \qquad [5.2]$$

where

$$q(t) = \gamma \int_0^t G(t')dt' \qquad [5.3]$$

is the dephasing function, $G(t)$ is the effective gradient waveform, and γ is the gyromagnetic ratio.

This model assumes that, although blood flow corresponds to motion on a larger scale than diffusion, the motion through the intricate capillary system is pseudorandom and mimics a diffusion process (referred to as pseudodiffusion). Taking this analogy even further, the psuedodiffusion coefficient can be modeled as $D^* = \bar{l}\bar{v}/6$, where $\bar{l}$ is the mean capillary segment length and $\bar{v}$ the mean blood velocity [102]. In other words, this assumption corresponds to the situation where blood water molecules change velocity (due to bends of capillaries) several times during the motion-encoding ('Model 1: Diffusive regime' in Fig. 5.1).

By acquiring the diffusion-signal at three or more different b-values, separate estimation of D_t and f is feasible based on the IVIM model [102]. The analysis can be performed in different ways, for example, by nonlinear fitting of Eq. 5.1 or step-wise analysis. Step-wise (or segmented/asymptotic) analysis is accomplished by first estimating D_t from high b-value data, and then estimating f (and sometimes D^*).

Spatially incoherent flow

Independently of the IVIM concept, Nalciouglu et al. derived a formalism for incoherent motion in terms of random directional flow [111]. They noted that, while mean bulk flow in a voxel gives rise to a net phase shift of the MR signal, random directional flow gives rise to an extra magnetization dephasing. This dephasing decreases the magnitude of the signal, and the size of the attenuation depends on the velocity distribution of the flowing spins. This concept can be used to model the effect of perfusion on the motion-encoded MRI signal, and Ahn et al. applied it to in vivo data to calculate 'capillary density maps' [112]. This model corresponds to the assumption that microvascular blood molecules flow in many different directions, but never change velocity during the motion-encoding period ('Model 2: Ballistic regime' in Fig. 5.1). Note that whereas the conventional IVIM model is focused on temporal incoherence, the random directional flow model is based purely on spatial incoherence.

Theory

Similarly to the diffusion weighting factor (b-value) used in diffusion MRI, the flow weighting factor α can be defined according to

$$\alpha = -\int_0^{T_E} q(t)dt = \gamma \int_0^{T_E} t\, G(t)dt, \qquad [5.4]$$

which specifies how sensitive the signal is to flow. If we consider a single tube with direction $\hat{k}$ in which particles flow with a velocity distribution $f_k(v)$, the signal attenuation due to the flow is given by [112]

$$F_{tube} = \int_{-\infty}^{\infty} f_k(v) e^{i\boldsymbol{\alpha} v \hat{k}} dv, \qquad [5.5]$$

where the flow weighting factor is written in bold typeface to signify that the encoding direction is preserved. Summing over all tubes in a voxel, and defining θ_k as the angle between $\boldsymbol{\alpha}$ and $\hat{k}$, we get the signal attenuation

$$F = \sum_k \int_{-\infty}^{\infty} f_k(v) e^{i\alpha v \cos\theta_k} dv = \int f(\theta) \left[\int_{-\infty}^{\infty} f(v) e^{i\alpha v \cos\theta} dv \right] d\theta, \qquad [5.6]$$

where the last sign of equality is based on the assumption of identical velocity distributions in all tubes, i.e., $f_k(v) = f(v)$, and $f(\theta)$ is the orientation distribution. For an isotropic orientation distribution, i.e., $f(\theta) = \sin(\theta)/2$ for $\theta \leq \pi$, the expression is further simplified to

$$F = \int_{-\infty}^{\infty} f(v)\,\mathrm{sinc}(\alpha v) dv, \qquad [5.7]$$

where $\mathrm{sinc}(x) = \sin(x)/x$. Equation 5.7 is a convenient expression from which analytical expressions can be derived for different velocity profiles. For example, plug flow with mean velocity v_0 yields a signal attenuation according to $F = \mathrm{sinc}(\alpha v_0)$, whereas laminar flow (parabolic profile) with mean velocity $v_0 = v_{max}/2$ yields $F = \mathrm{Si}(2\alpha v_0)/(2\alpha v_0)$, where Si is the sine integral [112].

In a slightly different approach, used in Paper v, it can be noted that a tube with mean velocity $\bar{\nu}_k$ contributes to the signal according to $e^{-i\varphi_k} = e^{-i\alpha\bar{\nu}_k}$, where φ_k is the cumulative phase for the entire tube. Summing over all tubes yields the signal attenuation according to

$$F = \sum_k e^{-i\alpha\bar{\nu}_k} = \int_{-\infty}^{\infty} f(\bar{\nu}) e^{-i\alpha\bar{v}} d\bar{\nu}, \qquad [5.8]$$

where $f(\bar{\nu})$ is the distribution of mean velocities. Equation 5.8 is also convenient, since we can choose the velocity distribution on a voxel level rather than specifying a global velocity profile. For example, a Gaussian velocity distribution with zero mean and width $\bar{v}$ yields an exponential signal attenuation according to $F = e^{-\alpha^2\langle\bar{v}^2\rangle/2}$ where $\langle\bar{v}^2\rangle$ is the average mean squared velocity [113]. A slight generalization of this attenuation factor was used in Paper v according to $F = e^{-\alpha^2 v_d^2}$ where v_d is a measure of velocity dispersion, which scales with velocity depending on the particular dispersion model, e.g., $v_d^2 = \langle\bar{v}^2\rangle/2$ for a Gaussian velocity distribution.

The same results can be obtained from both of the above approaches, in certain cases. For example, for a Gaussian velocity distribution on the voxel level $g(\bar{v})$, the corresponding tube velocity distribution is given by the Maxwell–Boltzmann distribution of speeds; $f(v) = 4\pi v^2 g(v)$.

General model and intermediate regime

The two models described above can be regarded as extreme cases of the same phenomenon which, by analogy to Brownian motion, can be referred to as the diffusive and ballistic

limits. From the perspective of turbulent flow studies, Kennan et al. suggested a general model for the effect of perfusion on motion-encoded MRI [113]. The model was derived from the concept of velocity autocorrelation, with a characteristic autocorrelation time T_0 describing the average time it takes for a blood particle to change velocity. The resulting equations were analogous to those of Stepišnik, derived from a frequency domain analysis of Brownian motion in the short-time limit [114]. The general model reduces to the models for the diffusive and ballistic limits when T_0 is very short or long compared to the encoding time, whereas the complete description can be used to characterize incoherent motion in the intermediate regime. Using IVIM data acquired with different encoding times, Wetscherek et al. found that microvascular blood flow in liver and pancreas was characterized as motion pertaining to the intermediate regime [115].

Flow compensated intravoxel incoherent motion

In the ballistic limit, signal loss due to spatially incoherent flow can be recovered using flow compensation. Ahn et al. exploited this fact to generate capillary density maps from the signal difference between a diffusion sequence with no flow compensation (NC) and a sequence with flow compensation (FC) , i.e., $S_{NC} - S_{FC}$ [112]. Maki et al. extended on this approach by acquiring NC and FC data with the same diffusion and relaxation weighting, and suggested the quantity $1 - S_{NC}/S_{FC}$ as a perfusion weighted map [116], whereas Fujita et al. applied the method of Ahn et al. and demonstrated in vivo brain results [117].

The FC is only complete if all blood particles move along straight lines during the encoding. The actual regime of the blood flow motion depends on the relation between T_0 and the total encoding time (observation time), which gives the researcher a certain degree of control in this regard. Hence, to shift the motion towards the ballistic limit, the encoding time was kept as short as possible in Paper v. Note that the relative amount of compensation (full, partial or none) observed in the data can potentially be used to infer the temporal regime of the motion.

Even though the IVIM and the spatially incoherent flow concepts were developed independently, they are basically two sides of the same coin (as described above). Thus, it seems reasonable to assume that also the IVIM technique might benefit from FC. The concept, presented in Paper v, is that joint analysis of NC and FC multi-b-value data should stabilize the fitting and yield improved IVIM parameter estimates. This approach can be interpreted as a multi-dimensional data collection and analysis, since both the diffusion weighting (b-value) and the flow weighting (α-value) is varied. The data were acquired using a single-refocused double diffusion encoding (DDE) sequence with bipolar gradient waveforms, which assured identical relaxation and diffusion weighting in the NC and FC data. Hence, the flow weighting varied with the diffusion weighting[2], and could be set to

[2]The use of more advanced gradient pulse designs would allow for independent variation of b- and α-values.

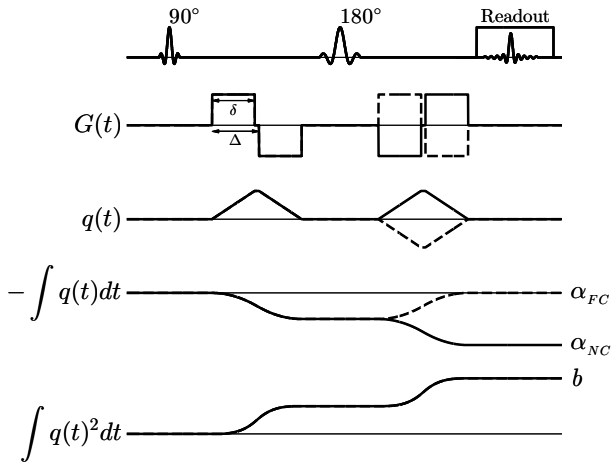

Figure 5.2: Scheme of the pulse sequence used in Paper v. The top row shows RF pulses and the signal readout, $G(t)$ is the gradient waveforms, $q(t)$ is the dephasing function (see Eq. 5.3), and the two bottom rows show the time-integrals that equals the flow weighting α and diffusion weigthing b at the time of acquisition (T_E). Solid and dashed lines corresponds to the NC and FC acquisitions, respectively.

zero by reversing the polarity of the second gradient block (Figure 5.2).

By assuming that the capillary blood flow pertains to the ballistic motion regime, the IVIM signal can be modeled according to

$$S(b,\alpha) = S_0 \left[(1-f)e^{-bD_t} + fe^{-bD_b} e^{-\alpha^2 v_d^2} \right], \qquad [5.9]$$

where D_b is the diffusion coefficient of blood, and $\alpha = 0$ for the FC acquisition. Comparing to the conventional IVIM model (Eq. 5.1), the pseudo-diffusion coefficient in the ballistic limit can be expressed as

$$D^* = D_b + \frac{\alpha^2}{b} v_d^2. \qquad [5.10]$$

This is an important relation since it shows that, for the ballistic limit, the pseudo-diffusion coefficient is dependent on the gradient pulses according to α^2/b, which can be optimized for increased sensitivity to flow.

Simulations suggested a distinct improvement in performance, in terms of accuracy and precision of IVIM parameter estimates, using the proposed technique. Brain data were acquired in healthy volunteers, and a clear rephasing effect was demonstrated, suggesting that the microvascular blood flow was closer to the ballistic limit than the diffusive limit, for an encoding time of 38 ms. Example data and corresponding model fits are shown in Figure 5.3.

In a related approach, Wetscherek et al. proposed to acquire NC and FC IVIM data with varied encoding times, and to include T_0 in the estimation [115]. Rather than deriving a model for the signal attenuation due to perfusion, they generated a library of phase

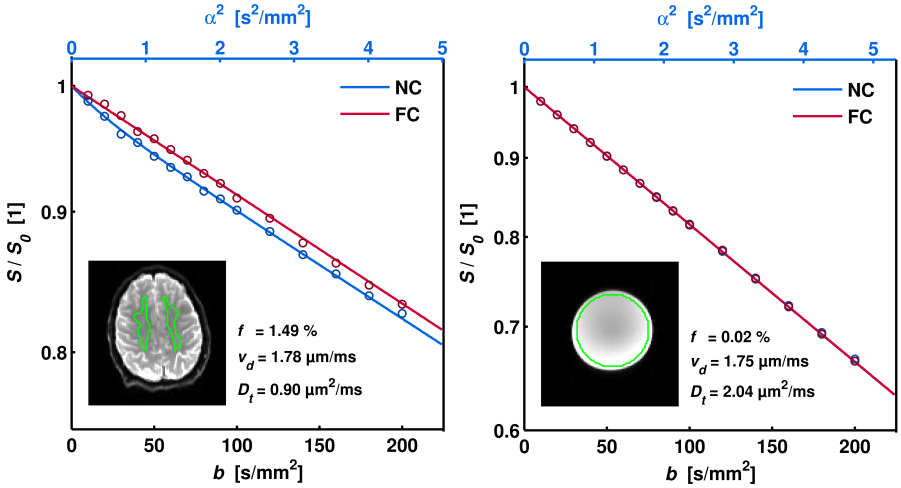

Figure 5.3: Example of results from Paper v. The left graph shows acquired in vivo data (circles) and the corresponding model fits (solid lines) for NC (blue) and FC (red), and the resulting IVIM parameter estimates. The data points originate from a WM ROI of a healthy volunteer, indicated in the inset figure. The graph to the right shows the corresponding information for a stationary water phantom. A clear rephasing effect was seen for the in vivo FC data, whereas the water phantom resulted in mono-exponential signal attenuation and no separation of the NC and FC data.

distributions from random-walk simulations, which was then fitted to the data. This approach is appealing because it does not rely on the assumption of a Gaussian phase distribution, and since it applies to motions pertaining to any temporal regime. On the other hand, a velocity profile still needs to be assumed, and the absence of an analytical signal model may impede the accessibility of the method.

Chapter 6

Conclusions and future aspects

Reliable quantitative MRI requires continuous development and improvement of the corresponding methods. This includes the entire process from data collection and sequence optimization, to method validation, data analysis approaches and interpretation of results. The current thesis presents novel implementations designed to improve measurements of perfusion and partial volumes in MRI. The doctoral projects have focused on testing the feasibility of the methods, and to assess the reliability of the output.

The methods presented in this work should primarily be viewed upon as basic MRI research, in the sense that the primary goal was to further develop and improve certain quantitative MRI techniques. A secondary goal was, obviously, that these techniques will yield value in clinical applications in the future. Accurate perfusion quantification is particularly important for certain clinical research questions, for example, in studies investigating the relation between regional perfusion levels and diseases, studies on global perfusion changes, or in longitudinal studies (e.g., in connection with monitoring or follow-up of various kinds of therapy). Reducing errors caused by arterial dispersion and delay, or related to various mathematical issues, is an important task in improving the interpretability of perfusion estimates. In addition to improving the perfusion estimates, such corrections also provide metrics related to the amount of delay and dispersion, which may show clinical value by themselves. The results of Paper I are encouraging in these aspects, and ASL is an especially attractive method since it is noninvasive. Although single time-point PCASL is the currently suggested ASL technique for clinical routine, time-resolved ASL is more robust in many situations and can provide additional information. Thus, time-resolved ASL is expected to be an important technique for certain applications also in the future. Furthermore, improved QUASAR variants with higher SNR are being developed [118], which make the present results important in guiding future research on model-free ASL.

The exact value of PVC in perfusion MRI is still a fairly open question, although it is clear that separation of the effects of intrinsic tissue perfusion and tissue volume enables improved parameter interpretation in cases where alteration of both quantities may be

present. Since PV-corrected perfusion values are less affected by variability in tissue content, they may also be more sensitive to perfusion changes and group-wise differences. Thus, PVC might become an essential part of perfusion MRI post-processing, at least for certain clinical questions. The FSM approach has been shown to be particularly suitable for PV mapping in low resolution native space. In Paper II, the obvious advantage of obtaining PV maps from the inherent ASL data was accompanied by a suggested improvement in PVC results. Furthermore, in Paper III, we demonstrated that PVEs are detectable and relevant also in DSC-MRI. These results constitute modest but important steps towards the establishment of PVC in perfusion MRI, which we expect will result in improved clinical information. Although we still lack a consensus with regard to which PVC algorithm to use, the most crucial question is arguably in which situations and applications that PVC will be most valuable.

The FSM technique is very new, and it is, at this point, difficult to determine its importance. It is indeed a very attractive method with great potential, especially since it is robust and simple. Apart from the potential to be used for conventional segmentation and volumetry applications, several studies have already employed FSM to improve different quantitative MRI methods. As an important step forward, in Paper IV, we suggested that the FSM concept can be adapted to different types of quantitative MRI data, and in Chapter 4, FSM was further generalized by the description of a comprehensive approach. This perspective of FSM being a general concept to which several different types of MRI sequences and data types can be applied opens up a slew of new possible implementations, and also emphasizes the potential of the method. The most obvious challenge is the determination of representative tissue parameters, but several improved approaches have already been proposed and this issue is expected to be further investigated in the future. Similarly, the particular model fitting approach is expected to be further improved.

A reliable noninvasive blood volume MRI technique remains to be recognized, but IVIM imaging is a important contender, although there are still challenges to address. The multi-dimensional approach described in Paper V enables a more robust analysis, and is thus an important part of the continued discussion on the possibilities of IVIM imaging. In particular, FC improved the accuracy and precision of the IVIM parameters, and in vivo data supported that many blood particles move along straight lines during the encoding. We believe that additional development of data acquisition, modeling and analysis will further improve the quality and interpretation of IVIM parameters. For example, temporal regime exploration, including autocorrelation time analysis, might provide new blood flow information and markers in the future.

The main conclusions of the papers included in this thesis were:

I. NSR deconvolution is feasible for model-free ASL, and improves residue function characterization and perfusion estimation.

II. PVs can be estimated from QUASAR ASL data, and used for subsequent PVC of perfusion values. Estimating PVs from data acquired with the same readout as the ASL data improves the output of the PVC, compared to using segmentation of a high resolution anatomical image.

III. PVEs are not negligible in DSC-MRI, and a simplified post-hoc PVC is feasible as a first-order approximation. A more elaborate PVC scheme is expected to furher improve the results.

IV. PV mapping using VFA-based FSM is feasible, and yields comparable results to IR-based FSM. The FSM approach is expected to gain more traction, because it yields robust PV maps with simple tools.

V. Cerebral microvascular blood flow is approximately ballistic for short encoding times. Joint analysis of NC and FC data stabilizes the IVIM analysis, and yields more robust and reliable parameter estimates.

Acknowledgements

There are many persons I would like to thank for their support of me and for the contributions to this work.

Thank you Linda — You've not only been the best main supervisor I could've wished for, but also my mentor, helping me to navigate in the confusing world of academia and research. Through major revisions, recommendation letters and happy hours, you've always been there. Thank you so much for believing in me, letting me try a lot of crazy ideas, and sending me across the globe to meet new friends and colleagues.

Thank you Ronnie — You are a true role model and an inspiration for this young (academically speaking) researcher. You unique and pseudo-down-to-earth perspective paints discussions with you in wonderful colors. Thank you for always taking the time to discuss the intricacies of obfuscated MR questions.

Thank you Freddy — I couldn't imagine a better research leader. You've tirelessly aided the larger picture of my progress, always in an enlightened and modest way. Thank you for being supportive of any and all ideas, and for truly caring about all of us in the MR physics group. Looking forward to the next dip in the ocean!

Thank you Esben for all the help and for being a great inspiration, the quasar is still shining. Thank you for the warm welcome in Utrecht, it was a fantastic time and great fun (except the hypercapnia challenge). As usual, the new PVC manuscript is almost done…

Thank you Kajsa, Samo, Daniel, Markus and Carl-Fredrik for letting me be part of your great efforts, and for teaching me in the black arts of diffusion MR. Great things comes from collaborations between different-minded people indeed. Vasco? Velo? What about BloodFlowComp (BloFloCo)?

Thank you all collaborators and co-authors — Thank you Emelie, Thijs, Fernando, Elna-Marie, Johan, David, and others. I am very happy to have had the pleasure to work with you!

Thank you the ASL community — It has been great getting to know so many in the friendly ASL research community. Special thanks to Xavier and the COST-AID for arranging meetings and stimulating collaborations.

Thank you all colleagues — Thank you Filip, Mikael, Gustav, Johan, Anna et al. for all the fun at and away from work. Thank you all classmates, fellow PhD students, seniors and others at MSF for making up a great department. Thank you to the amazing colleagues at

SUS, for always being helpful. Thank you everybody in, and affiliated with, the MR physics group — it is a privilege to be part of a group with such amazing people!

Thank you my friends — The Hässleholm gang (you're the best), the Lunda gang (you're the coolest), as well as old and new friends — thank you for the support, and for being fine with that I do 'something with MRI'.

Thank you my family — Warmest thanks to my amazing family. Thank you for always supporting me and encouraging me to go my own way.

Thank you Sandra — Thank you for all the support and love, and for being my best friend. I am so lucky to have you and your family in my life.

References

[1] Tofts PS. Concepts: Measurement and MR. In P Tofts, ed., Quantitative MRI of the Brain, John Wiley & Sons, Ltd, Chichester, 2003, pp. 1–15.

[2] Calamante F, Thomas DL, Pell GS, Wiersma J, Turner R. Measuring cerebral blood flow using magnetic resonance imaging techniques. J Cereb Blood Flow Metab 1999; 19(7):701–735.

[3] Barbier EL, Lamalle L, Décorps M. Methodology of brain perfusion imaging. J Magn Reson Imaging 2001;13(4):496–520.

[4] O'Connor JPB, Tofts PS, Miles KA, Parkes LM, Thompson G, Jackson A. Dynamic contrast-enhanced imaging techniques: CT and MRI. Br J Radiol 2011;84(SI2):S112–S120.

[5] Wirestam R. Using contrast agents to obtain maps of regional perfusion and capillary wall permeability. Imaging Med 2012;4(4):423–442.

[6] Barker PB, Golay X, Zaharchuk G, eds. Clinical perfusion MRI: Techniques and applications. Cambridge University Press, Cambridge, 2013.

[7] Jahng GH, Li KL, Østergaard L, Calamante F. Perfusion magnetic resonance imaging: A comprehensive update on principles and techniques. Korean J Radiol 2014;15(5):554.

[8] Kety SS, Schmidt CF. The determination of cerebral blood flow in man by the use of nitrous oxide in low concentrations. Am J Physiol Content 1945;143(1):53–66.

[9] Meier P, Zierler KL. On the theory of the indicator-dilution method for measurement of blood flow and volume. J Appl Physiol 1954;6(12):731–744.

[10] Zierler KL. Theoretical basis of indicator-dilution methods for measuring flow and volume. Circ Res 1962;10(3):393–407.

[11] Zierler KL. Equations for measuring blood flow by external monitoring of radioisotopes. Circ Res 1965;16(4):309–321.

[12] Fieselmann A, Kowarschik M, Ganguly A, Hornegger J, Fahrig R. Deconvolution-based CT and MR brain perfusion measurement: Theoretical model revisited and practical implementation details. Int J Biomed Imaging 2011;2011:1–20.

[13] Lassen NA, Perl W. Tracer kinetic methods in medical physiology. Raven Press, New York, 1979, p. 122 & 144.

[14] Axel L. Cerebral blood flow determination by rapid-sequence computed tomography: Theoretical analysis. Radiology 1980;137(3):679–686.

[15] Axel L. Tissue mean transit time from dynamic computed tomography by a simple deconvolution technique. Invest Radiol 1983;18(1):94–99.

[16] Stewart GN. Researches on the circulation time in organs and on the influences which affect it: Parts I—III. J Physiol 1893;15(1-2):1.

[17] Villringer A, Rosen BR, Belliveau JW, Ackerman JL, Lauffer RB, Buxton RB, Chao YS, Wedeenand VJ, Brady TJ. Dynamic imaging with lanthanide chelates in normal brain: Contrast due to magnetic susceptibility effects. Magn Reson Med 1988;6(2):164–174.

[18] Rosen BR, Belliveau JW, Chien D. Perfusion imaging by nuclear magnetic resonance. Magn Reson Q 1989;5(4):263–281.

[19] Rosen BR, Belliveau JW, Vevea JM, Brady TJ. Perfusion imaging with NMR contrast agents. Magn Reson Med 1990;14(2):249–265.

[20] Rempp KA, Brix G, Wenz F, Becker CR, Gückel F, Lorenz WJ. Quantification of regional cerebral blood flow and volume with dynamic susceptibility contrast-enhanced MR imaging. Radiology 1994;193(3):637–641.

[21] Østergaard L, Weisskoff RM, Chesler DA, Gyldensted C, Rosen BR. High resolution measurement of cerebral blood flow using intravascular tracer bolus passages. Part I: Mathematical approach and statistical analysis. Magn Reson Med 1996;36(5):715–725.

[22] Østergaard L, Sorensen AG, Kwong KK, Weisskoff RM, Gyldensted C, Rosen BR. High resolution measurement of cerebral blood flow using intravascular tracer bolus passages. Part II: Experimental comparison and preliminary results. Magn Reson Med 1996; 36(5):726–736.

[23] Østergaard L. Principles of cerebral perfusion imaging by bolus tracking. J Magn Reson Imaging 2005;22(6):710–717.

[24] Knutsson L, Ståhlberg F, Wirestam R. Absolute quantification of perfusion using dynamic susceptibility contrast MRI: Pitfalls and possibilities. Magn Reson Mater Phy 2010; 23(1):1–21.

[25] Kiselev V. On the theoretical basis of perfusion measurements by dynamic susceptibility contrast MRI. Magn Reson Med 2001;46(6):1113–1122.

[26] Kjølby BF, Østergaard L, Kiselev VG. Theoretical model of intravascular paramagnetic tracers effect on tissue relaxation. Magn Reson Med 2006;56(1):187–197.

[27] Calamante F. Arterial input function in perfusion MRI: A comprehensive review. Prog Nucl Magn Reson Spectrosc 2013;74:1–32.

[28] Calamante F, Connelly A, van Osch MJ. Nonlinear ΔR^*2 effects in perfusion quantification using bolus-tracking MRI. Magn Reson Med 2009;61(2):486–492.

[29] Knutsson L, Lindgren E, Ahlgren A, van Osch MJ, Markenroth Bloch K, Surova Y, Ståhlberg F, van Westen D, Wirestam R. Reduction of arterial partial volume effects for improved absolute quantification of DSC-MRI perfusion estimates: Comparison between tail scaling and prebolus administration. J Magn Reson Imaging 2015;41(4):903–908.

[30] Lindgren E, Wirestam R, Markenroth Bloch K, Ahlgren A, van Osch MJP, van Westen D, Surova Y, Ståhlberg F, Knutsson L. Absolute quantification of perfusion by dynamic susceptibility contrast MRI using Bookend and VASO steady-state CBV calibration: A comparison with pseudo-continuous ASL. Magn Reson Mater Phy 2014;27(6):487–499.

[31] Calamante F, Gadian DG, Connelly A. Delay and dispersion effects in dynamic susceptibility contrast MRI: Simulations using singular value decomposition. Magn Reson Med 2000; 44(3):466–473.

[32] Knutsson L, Larsson EM, Thilmann O, Ståhlberg F, Wirestam R. Calculation of cerebral perfusion parameters using regional arterial input functions identified by factor analysis. J Magn Reson Imaging 2006;23(4):444–453.

[33] Willats L, Christensen S, Ma HK, Donnan GA, Connelly A, Calamante F. Validating a local arterial input function method for improved perfusion quantification in stroke. J Cereb Blood Flow Metab 2011;31(11):2189–2198.

[34] Willats L, Connelly A, Calamante F. Improved deconvolution of perfusion MRI data in the presence of bolus delay and dispersion. Magn Reson Med 2006;56(1):146–156.

[35] Willats L, Connelly A, Calamante F. Minimising the effects of bolus dispersion in bolus-tracking MRI. NMR Biomed 2008;21(10):1126–1137.

[36] Zanderigo F, Bertoldo A, Pillonetto G, Cobelli$^{ast\$}$ C. Nonlinear stochastic regularization to characterize tissue residue function in bolus-tracking MRI: Assessment and comparison with SVD, block-circulant SVD, and Tikhonov. IEEE Trans Biomed Eng 2009;56(5):1287–1297.

[37] Mouannes-Srour JJ, Shin W, Ansari SA, Hurley MC, Vakil P, Bendok BR, Lee JL, Derdeyn CP, Carroll TJ. Correction for arterial-tissue delay and dispersion in absolute quantitative cerebral perfusion DSC MR imaging. Magnetic Resonance Medicine 2012;68(2):495–506.

[38] Mehndiratta A, Calamante F, MacIntosh BJ, Crane DE, Payne SJ, Chappell MA. Modeling and correction of bolus dispersion effects in dynamic susceptibility contrast MRI. Magn Reson Med 2014;72(6):1762–1774.

[39] Hrabe J, Lewis DP. Two analytical solutions for a model of pulsed arterial spin labeling with randomized blood arrival times. J Magn Reson 2004;167(1):49–55.

[40] Ozyurt O, Dincer A, Ozturk C. A modified version of Hrabe-Lewis model to account dispersion of labeled bolus in arterial spin labeling. Proc Intl Soc Mag Reson Med 2010; 18:4065.

[41] Chappell MA, Woolrich MW, Kazan S, Jezzard P, Payne SJ, MacIntosh BJ. Modeling dispersion in arterial spin labeling: Validation using dynamic angiographic measurements. Magn Reson Med 2013;69(2):563–570.

[42] Weisskoff RM, Chesler D, Boxerman JL, Rosen BR. Pitfalls in MR measurement of tissue blood flow with intravascular tracers: Which mean transit time? Magn Reson Med 1993; 29(4):553–558.

[43] Perthen JE, Calamante F, Gadian DG, Connelly A. Is quantification of bolus tracking MRI reliable without deconvolution? Magn Reson Med 2002;47(1):61–67.

[44] Mouridsen K, Friston K, Hjort N, Gyldensted L, Østergaard L, Kiebel S. Bayesian estimation of cerebral perfusion using a physiological model of microvasculature. NeuroImage 2006; 33(2):570–579.

[45] Wirestam R, Ståhlberg F. Wavelet-based noise reduction for improved deconvolution of time-series data in dynamic susceptibility-contrast MRI. Magn Reson Mater Phy 2005; 18(3):113–118.

[46] Calamante F, Gadian DG, Connelly A. Quantification of bolus-tracking MRI: Improved characterization of the tissue residue function using Tikhonov regularization. Magn Reson Med 2003;50(6):1237–1247.

[47] Wu O, Østergaard L, Weisskoff RM, Benner T, Rosen BR, Sorensen AG. Tracer arrival timing-insensitive technique for estimating flow in MR perfusion-weighted imaging using singular value decomposition with a block-circulant deconvolution matrix. Magn Reson Med 2003;50(1):164–174.

[48] Mehndiratta A, MacIntosh BJ, Crane DE, Payne SJ, Chappell MA. A control point interpolation method for the non-parametric quantification of cerebral haemodynamics from dynamic susceptibility contrast MRI. NeuroImage 2013;64:560–570.

[49] Ahlgren A, Wirestam R, Ståhlberg F, Knutsson L. Bézier curve deconvolution for model-free quantification of cerebral perfusion. Proc Intl Soc Mag Reson Med 2016;24:647.

[50] Detre JA, Leigh JS, Williams DS, Koretsky AP. Perfusion imaging. Magn Reson Med 1992; 23(1):37–45.

[51] Williams DS, Detre JA, Leigh JS, Koretsky AP. Magnetic resonance imaging of perfusion using spin inversion of arterial water. Proc Natl Acad Sci USA 1992;89(1):212–216.

[52] Edelman RR, Siewert B, Darby DG, Thangaraj V, Nobre AC, Mesulam MM, Warach S. Qualitative mapping of cerebral blood flow and functional localization with echo-planar MR imaging and signal targeting with alternating radio frequency. Radiology 1994; 192(2):513–520.

[53] Dai W, Garcia D, de Bazelaire C, Alsop DC. Continuous flow-driven inversion for arterial spin labeling using pulsed radio frequency and gradient fields. Magn Reson Med 2008; 60(6):1488–1497.

[54] Wu WC, Fernández-Seara M, Detre JA, Wehrli FW, Wang J. A theoretical and experimental investigation of the tagging efficiency of pseudocontinuous arterial spin labeling. Magn Reson Med 2007;58(5):1020–1027.

[55] Alsop DC, Detre JA, Golay X, Günther M, Hendrikse J, Hernandez-Garcia L, Lu H, MacIntosh BJ, Parkes LM, Smits M, others. Recommended implementation of arterial spin-labeled perfusion MRI for clinical applications: A consensus of the ISMRM perfusion study group and the European consortium for ASL in dementia. Magn Reson Med 2015; 73(1):102–116.

[56] Buxton RB, Frank LR, Wong EC, Siewert B, Warach S, Edelman RR. A general kinetic model for quantitative perfusion imaging with arterial spin labeling. Magn Reson Med 1998; 40(3):383–396.

[57] Petersen ET, Zimine I, Ho YCL, Golay X. Non-invasive measurement of perfusion: A critical review of arterial spin labelling techniques. Br J Radiol 2006;79(944):688–701.

[58] Petersen ET, Lim T, Golay X. Model-free arterial spin labeling quantification approach for perfusion MRI. Magn Reson Med 2006;55(2):219–232.

[59] Petersen ET, Mouridsen K, Golay X. The QUASAR reproducibility study, Part II: Results from a multi-center arterial spin labeling test–retest study. NeuroImage 2010;49(1):104–113.

[60] Petersen ET. Brain perfusion imaging: Quantification of cerebral blood flow using ASL techniques. Doctoral thesis, Aarhus University, Aarhus, 2009.

[61] González Ballester MÁ, Zisserman AP, Brady M. Estimation of the partial volume effect in MRI. Medical Image Analysis 2002;6(4):389–405.

[62] Tohka J. Partial volume effect modeling for segmentation and tissue classification of brain magnetic resonance images: A review. World J Radiol 2014;6(11):855.

[63] Clarke LP, Velthuizen RP, Camacho MA, Heine JJ, Vaidyanathan M, Hall LO, Thatcher RW, Silbiger ML. MRI segmentation: Methods and applications. Magn Reson Imaging 1995;13(3):343–368.

[64] Wang L, Chitiboi T, Meine H, Günther M, Hahn HK. Principles and methods for automatic and semi-automatic tissue segmentation in MRI data. Magn Reson Mater Phy 2016; 29(2):95–110.

[65] Helms G. Segmentation of human brain using structural MRI. Magn Reson Mater Phy 2016;29(2):111–124.

[66] Kao YH, Sorenson JA, Winkler SS. MR image segmentation using vector decomposition and probability techniques: A general model and its application to dual-echo images. Magn Reson Med 1996;35(1):114–125.

[67] Alfano B, Brunetti A, Covelli EM, Quarantelli M, Panico MR, Ciarmiello A, Salvatore M. Unsupervised, automated segmentation of the normal brain using a multispectral relaxometric magnetic resonance approach. Magn Reson Med 1997;37(1):84–93.

[68] Liu T, Li H, Wong K, Tarokh A, Guo L, Wong STC. Brain tissue segmentation based on DTI data. NeuroImage 2007;38(1):114–123.

[69] West J, Warntjes JBM, Lundberg P. Novel whole brain segmentation and volume estimation using quantitative MRI. Eur Radiol 2012;22(5):998–1007.

[70] Choi HS, Haynor DR, Kim Y. Partial volume tissue classification of multichannel magnetic resonance images-a mixel model. IEEE Trans Med Imaging 1991;10(3):395–407.

[71] Cabezas M, Oliver A, Lladó X, Freixenet J, Bach Cuadra M. A review of atlas-based segmentation for magnetic resonance brain images. Comput Methods Programs Biomed 2011;104(3):e158–e177.

[72] Ashburner J, Friston KJ. Unified segmentation. NeuroImage 2005;26(3):839–851.

[73] Bedell BJ, Narayana PA. Volumetric analysis of white matter, gray matter, and CSF using fractional volume analysis. Magn Reson Med 1998;39(6):961–969.

[74] Ruan S, Jaggi C, Xue J, Fadili J, Bloyet D. Brain tissue classification of magnetic resonance images using partial volume modeling. IEEE Trans Med Imaging 2000;19(12):1179–1187.

[75] Shattuck DW, Sandor-Leahy SR, Schaper KA, Rottenberg DA, Leahy RM. Magnetic resonance image tissue classification using a partial volume model. NeuroImage 2001; 13(5):856–876.

[76] Keller SS, Roberts N. Measurement of brain volume using MRI: Software, techniques, choices and prerequisites. J Anthr Sci 2009;87:127–151.

[77] Schmitter D, Roche A, Maréchal B, Ribes D, Abdulkadir A, Bach-Cuadra M, Daducci A, Granziera C, Klöppel S, Maeder P, Meuli R, Krueger G. An evaluation of volume-based morphometry for prediction of mild cognitive impairment and Alzheimer's disease. NeuroImage Clin 2015;7:7–17.

[78] Shin W, Geng X, Gu H, Zhan W, Zou Q, Yang Y. Automated brain tissue segmentation based on fractional signal mapping from inversion recovery Look–Locker acquisition. NeuroImage 2010;52(4):1347–1354.

[79] Petr J, Schramm G, Hofheinz F, Langner J, van den Hoff J. Partial volume correction in arterial spin labeling using a Look-Locker sequence. Magn Reson Med 2013; 70(6):1535–1543.

[80] Oliver RA. Improved quantification of arterial spin labelling images using partial volume correction techniques. Doctoral thesis, University College London, London, 2015.

[81] Huber L, Goense J, Kennerley AJ, Ivanov D, Krieger SN, Lepsien J, Trampel R, Turner R, Möller HE. Investigation of the neurovascular coupling in positive and negative BOLD responses in human brain at 7T. NeuroImage 2014;97:349–362.

[82] Huber L, Ivanov D, Krieger SN, Streicher MN, Mildner T, Poser BA, Möller HE, Turner R. Slab-selective, BOLD-corrected VASO at 7 Tesla provides measures of cerebral blood volume reactivity with high signal-to-noise ratio. Magn Reson Med 2014;72(1):137–148.

[83] Christensen KA, Grant DM, Schulman EM, Walling C. Optimal determination of relaxation times of Fourier transform nuclear magnetic resonance. Determination of spin-lattice relaxation times in chemically polarized species. J Phys Chem 1974;78(19):1971–1977.

[84] Fram EK, Herfkens RJ, Johnson GA, Glover GH, Karis JP, Shimakawa A, Perkins TG, Pelc NJ. Rapid calculation of T1 using variable flip angle gradient refocused imaging. Magnetic Resonance Imaging 1987;5(3):201–208.

[85] Maier SE, Vajapeyam S, Mamata H, Westin CF, Jolesz FA, Mulkern RV. Biexponential diffusion tensor analysis of human brain diffusion data. Magn Reson Med 2004; 51(2):321–330.

[86] Pasternak O, Sochen N, Gur Y, Intrator N, Assaf Y. Free water elimination and mapping from diffusion MRI. Magn Reson Med 2009;62(3):717–730.

[87] Zhang H, Schneider T, Wheeler-Kingshott CA, Alexander DC. NODDI: Practical in vivo neurite orientation dispersion and density imaging of the human brain. NeuroImage 2012; 61(4):1000–1016.

[88] Erlandsson K, Buvat I, Pretorius PH, Thomas BA, Hutton BF. A review of partial volume correction techniques for emission tomography and their applications in neurology, cardiology and oncology. Phys Med Biol 2012;57(21):R119.

[89] Asllani I, Borogovac A, Brown TR. Regression algorithm correcting for partial volume effects in arterial spin labeling MRI. Magn Reson Med 2008;60(6):1362–1371.

[90] Chappell MA, Groves AR, MacIntosh BJ, Donahue MJ, Jezzard P, Woolrich MW. Partial volume correction of multiple inversion time arterial spin labeling MRI data. Magn Reson Med 2011;65(4):1173–1183.

[91] Asllani I, Habeck C, Borogovac A, Brown TR, Brickman AM, Stern Y. Separating function from structure in perfusion imaging of the aging brain. Hum Brain Mapp 2009; 30(9):2927–2935.

[92] Binnewijzend MA, Kuijer JP, Benedictus MR, van der Flier WM, Wink AM, Wattjes MP, van Berckel BN, Scheltens P, Barkhof F. Cerebral blood flow measured with 3D pseudocontinuous arterial spin-labeling MR imaging in Alzheimer disease and mild cognitive impairment: A marker for disease severity. Radiology 2013;267(1):221–230.

[93] Borogovac A, Habeck C, Small SA, Asllani I. Mapping brain function using a 30-day interval between baseline and activation: A novel arterial spin labeling fMRI approach. J Cereb Blood Flow Metab 2010;30(10):1721–1733.

[94] Meltzer CC, Cantwell MN, Greer PJ, Ben-Eliezer D, Smith G, Frank G, Kaye WH, Houck PR, Price JC. Does cerebral blood flow decline in healthy aging? A PET study with partial-volume correction. J Nucl Med 2000;41(11):1842–1848.

[95] Hutton BF, Thomas BA, Erlandsson K, Bousse A, Reilhac-Laborde A, Kazantsev D, Pedemonte S, Vunckx K, Arridge SR, Ourselin S. What approach to brain partial volume correction is best for PET/MRI? Nucl Instrum Meth A 2013;702:29–33.

[96] Johnson NA, Jahng GH, Weiner MW, Miller BL, Chui HC, Jagust WJ, Gorno-Tempini ML, Schuff N. Pattern of cerebral hypoperfusion in Alzheimer disease and mild cognitive impairment measured with arterial spin-labeling MR imaging: Initial experience. Radiology 2005;234(3):851–859.

[97] Liang X, Connelly A, Calamante F. Improved partial volume correction for single inversion time arterial spin labeling data. Magn Reson Med 2013;69(2):531–537.

[98] Liu Y, Li B, Zhang X, Zhang L, Liang Z, Lu H. Partial volume correction for arterial spin labeling data using spatial-temporal information. Proc SPIE Med Imaging 2015; 9413:941325.

[99] Kuijer JP, de Sitter A, Binnewijzend MA, Barkhof F, Verdaasdonk RM. Consistency checks for partial volume correction of ASL perfusion maps. Proc Intl Soc Mag Reson Med 2014; 22:2712.

[100] Petr J, Mutsaerts HJ, De Vita E, Maus J, Jörg vdH, Asllani I. Deformation and resolution issues in partial volume correction of 2D arterial spin labeling data. Proc Intl Soc Mag Reson Med 2016;24:1496.

[101] Le Bihan D, Breton E, Lallemand D, Grenier P, Cabanis E, Laval-Jeantet M. MR imaging of intravoxel incoherent motions: Application to diffusion and perfusion in neurologic disorders. Radiology 1986;161(2):401–407.

[102] Le Bihan D, Breton E, Lallemand D, Aubin ML, Vignaud J, Laval-Jeantet M. Separation of diffusion and perfusion in intravoxel incoherent motion MR imaging. Radiology 1988; 168(2):497–505.

[103] Henkelman RM. Does IVIM measure classical perfusion? Magn Reson Med 1990; 16(3):470–475.

[104] Le Bihan D, Turner R. The capillary network: A link between IVIM and classical perfusion. Magn Reson Med 1992;27(1):171–178.

[105] Wirestam R, Borg M, Brockstedt S, Lindgren A, Holtås S, Ståhlberg F. Perfusion-related parameters in intravoxel incoherent motion MR imaging compared with CBV and CBF measured by dynamic susceptibility-contrast MR technique. Acta Radiol 2001; 42(2):123–128.

[106] Koh DM, Collins DJ, Orton MR. Intravoxel incoherent motion in body diffusion-weighted MRI: Reality and challenges. American Journal of Roentgenology 2011;196(6):1351–1361.

[107] Federau C, O'Brien K, Meuli R, Hagmann P, Maeder P. Measuring brain perfusion with intravoxel incoherent motion (IVIM): Initial clinical experience. J Magn Reson Imaging 2014;39(3):624–632.

[108] Le Bihan D, Turner R, Moonen CTW, Pekar J. Imaging of diffusion and microcirculation with gradient sensitization: Design, strategy, and significance. J Magn Reson Imaging 1991; 1(1):7–28.

[109] Pekar J, Moonen CTW, van Zijl PCM. On the precision of diffusion/perfusion imaging by gradient sensitization. Magn Reson Med 1992;23(1):122–129.

[110] Lemke A, Laun FB, Simon D, Stieltjes B, Schad LR. An in vivo verification of the intravoxel incoherent motion effect in diffusion-weighted imaging of the abdomen. Magn Reson Med 2010;64(6):1580–1585.

[111] Nalcioglu O, Cho ZH. Measurement of bulk and random directional velocity fields by NMR imaging. IEEE Trans Med Imaging 1987;6(4):356–359.

[112] Ahn CB, Lee SY, Nalcioglu O, Cho ZH. The effects of random directional distributed flow in nuclear magnetic resonance imaging. Med Phys 1987;14(1):43–48.

[113] Kennan RP. A general model of microcirculatory blood flow effects in gradient sensitized MRI. Med Phys 1994;21(4):539.

[114] Stepišnik J. NMR measurement and Brownian movement in the short-time limit. Phys B Condens Matter 1994;198(4):299–306.

[115] Wetscherek A, Stieltjes B, Laun FB. Flow-compensated intravoxel incoherent motion diffusion imaging. Magn Reson Med 2015;74(2):410–419.

[116] Maki JH, Macfall JR, Johnson GA. The use of gradient flow compensation to separate diffusion and microcirculatory flow in MRI. Magn Reson Med 1991;17(1):95–107.

[117] Fujita N, Harada K, Sakurai K, Akai Y, Kozuka T. Separation of diffusion and slow flow effects by use of flow rephasing and dephasing. Magn Reson Med 1992;24(1):109–122.

[118] Petersen ET, De Vis JB, Cornelis AT vdB, Hendrikse J. Turbo-QUASAR: A signal-to-noise optimal arterial spin labeling and sampling strategy. Proc Intl Soc Mag Reson Med 2013; 21:2146.

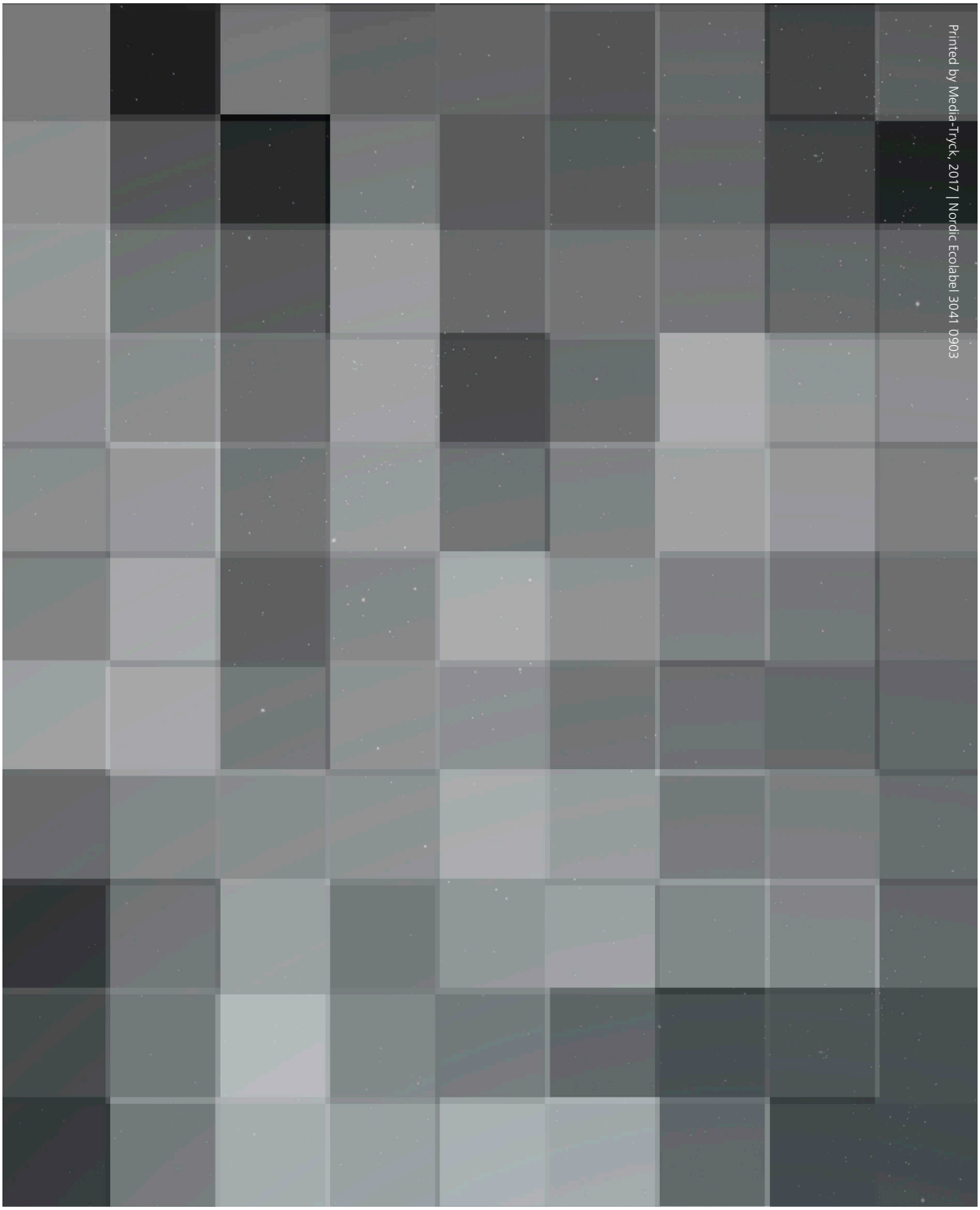

Printed by Media-Tryck, 2017 | Nordic Ecolabel 3041 0903

LUND UNIVERSITY

Faculty of Science,
Department of Medical Radiation Physics
ISBN 978-91-7753-098-5